

Master Thesis

INNOVATIVE SUNLIGHT DRIVEN  
THERMAL STORAGE SLURRY FOR  
DIRECT ABSORPTION SOLAR  
COLLECTORS (DASC).

Rakshith Mukkatira Chengappa

S1893920

For the CTW Faculty at the University of Twente

Thermal Engineering

2019

EXAMINATION COMMITTEE

Prof. Ir. Theo Van der Meer (chairman)

Dr. Mina Shahi (Supervisor)

Dr. Mohammad Mehrali (Supervisor)

Dr.Ir. N.P. Kruyt (External member)

UNIVERSITY OF TWENTE.



## Summary

The solar energy is available freely in nature. Traditionally solar thermal receivers are used to utilize this carbon neutral energy. With recent advances in technology to improve the efficiency, and overcome the heating losses in the existing collectors, a new technology called Direct Absorption Solar Collector (DASC) is proposed. In this technology, the solar energy is directly absorbed and transferred by the working fluid. To overcome the time mismatch between availability and demand of solar irradiation, Phase Change Materials (PCMs) are added to the heat carrier. In this way, the latent heat can be exploited in combination with the sensible heat of the carrier itself. This innovative thermal storage slurry for DASC is in research phase but has numerous implications in building heating/cooling systems, thermal storage, and thermal regulating fabric.

In this thesis, the objectives are 1- to design and install a laboratory scale stationary state DASC with simulated radiation source; 2-to examine the photo-thermal as well as thermal storage performance of the slurries; 3- to study the effect of different parameters like collector height, irradiation time on the collector efficiency when using PCM slurries.

The PCM slurries used in this study contain different concentrations of palmitic acid/silicon-di-oxide and carbon black nanoparticles suspended in the pure water. The performance of the slurry in comparison to the pure water depends on the collector height and irradiation time. This study shows that for a receiver with the height of 13.5mm and radiation time of approximately one hour, the efficiency is 7.7% higher compared to that of water. In addition, for this slurry due to the introduction of latent heat thermal storage material along with carbon particles, there is an improvement of about 8.3% in the thermal storage density compared to water.

## Preface

This report is written for attaining the master's degree in Mechanical Engineering at the University of Twente. Thermal storage slurry for direct absorption solar collector is the research topic.

Firstly, I would like to thank Dr. Mina Shahi, who allowed me to work on this project. I very much appreciate her positive attitude, timely advice, encouragement, and feedback to improve during our meeting.

I express my warmest gratitude to my daily supervisor, Dr. Mohammad Mehrali, to whom I am so much indebted. His constant support, discussion, and guidance are appreciated.

This thesis consists of a design process and experimental work in the Thermal Engineering Laboratory. The experiments would not be possible to perform without the help of Henk-Jan Moed and Robert, special thanks to them. I would also like to extend my acknowledgment to the people of the design lab for helping me with the 3D printing.

I want to express my gratitude for the support and guidance given by Dr. Sara Tahan Latibari during the initial phase of the project.

I thankfully acknowledge Prof. Theo van der Meer for his comments, and suggestions which helped me improve the readability of the thesis.

I would also like to thank the engineering technology faculty of the University of Twente for their kindness and administrative support.

I am forever thankful to my friends in helping me in all aspects of life. Finally, I wholeheartedly appreciate my family members for their endless love and support. I am forever indebted to my parents for giving me the opportunity and encouragement to explore new directions in life.

# Table of Contents

Summary .....	i
Preface.....	ii
List of Figures .....	v
List of Tables .....	vi
Nomenclature .....	vii
Chapter 1 .....	2
Introduction .....	2
1.1 Background.....	2
1.2 Non-concentrating solar thermal collectors .....	4
1.3 Nanofluids .....	5
1.4 Phase change material (PCM) slurries .....	6
1.5 Research goals .....	7
1.6 Outline of the thesis .....	7
Chapter 2.....	8
Methodology.....	8
2.1 Working concept/ theory.....	8
2.2 Experimental setup .....	12
2.2.1 Solar Simulator .....	12
2.2.2 Quartz window .....	14
2.2.3 Collector.....	14
2.2.4 Thermometers .....	16
2.2.5 Data Acquisition system (DAQ).....	16
2.3 Instrument calibration.....	18
2.3.1 Solar simulator setup fine-tuning.....	18
2.3.2 Thermometer calibration .....	19
2.4 Working fluids .....	20
2.4.1 Preparation and characterization .....	20
2.5 Experimental procedure .....	21
2.5.1 Instrument phase .....	21
2.5.2 Sample phase.....	22
Chapter 3.....	24
Results and Discussion.....	24
3.1 Temperature distributions.....	24

3.2 Efficiency.....	33
3.3 Thermal storage .....	38
Chapter 4 .....	41
Conclusions and Recommendations .....	41
4.1 Conclusions.....	41
4.2 Recommendations .....	42
References .....	43
Appendix A1.....	47
Solar Simulator .....	47
Appendix A2.....	51
Other Components.....	51
Appendix A3.....	55
Materials.....	55

## List of Figures

Figure 1.1: Solar energy availability[18].	3
Figure 1.2: Solar thermal collectors general classification [21].	4
Figure 2.1: Concept of photothermal slurries.	8
Figure 2.2: The working concept of photothermal slurries in DASC.	9
Figure 2.3: Schematic of Direct Absorption Solar Collector experimental setup.	12
Figure 2.4: a) Dimensions in mm and other details of the collector. b) 3D printed collector.	15
Figure 2.5: The collector design process.	16
Figure 2.6: Data acquisition system.	17
Figure 2.7: Installed solar simulator.	17
Figure 2.8: Intensity measurement points for the non-uniformity profile.	18
Figure 2.9: a) Intensity (optical center) vs height for different power. b) Non-uniformity as a function of height and power.	18
Figure 2.10: Temperature voltage calibration curve.	19
Figure 2.11: Samples used in the photothermal experiment.	20
Figure 2.12: Instrument phase schematic.	22
Figure 2.13: Sample phase schematic.	23
Figure 3.1: Average temperature measured for base fluid (water) at 1 sun irradiation.	24
Figure 3.2: Average temperature as a function of time at 1 Sun irradiation for carbon black 45PPM.	25
Figure 3.3: Average temperature as a function of time with 1 Sun irradiation for <i>PA/SiO<sub>2</sub></i> 10wt%-45PPM.	26
Figure 3.4: Average temperature as a function of time with 1 Sun irradiation of <i>PA/SiO<sub>2</sub></i> 10wt% 45PPM till 25000s.	27
Figure 3.5: Temperature profiles at different heights and time up to 3000s; for a)base fluid - water, b)CB 25PPM, c)CB 35PPM, d) <i>Pa/SiO<sub>2</sub></i> 2wt%, e) <i>PA/SiO<sub>2</sub></i> 2wt%-9PPM CB, f) <i>PA/SiO<sub>2</sub></i> -4wt% 18PPM CB.	28
Figure 3.6: Temperature as a function of time, for different samples at $y/H=0.05$ .	29
Figure 3.7: Average temperature as a function of time, for different samples at $y/H=1$ .	30
Figure 3.8: Temperature variation with depth at the irradiation time of a)600s, b)3000s, c) 3600s, d)7200s, e) 9000s.	32
Figure 3.9: Collector efficiencies as a function of collector height and irradiation time for a) base fluid, b) CB 25PPM, c) CB 35PPM, d) <i>Pa/SiO<sub>2</sub></i> 2wt%, e) <i>Pa/SiO<sub>2</sub></i> 2wt%- 9PPM CB, f) <i>Pa/SiO<sub>2</sub></i> 4wt%-18PPM CB.	34
Figure 3.10: Collector efficiency as a function of irradiation time for different samples at height a) $y/H = 0.05$ and b) $y/H = 1$ .	35
Figure 3.11: Collector efficiency as a function of height for water, <i>Pa/SiO<sub>2</sub></i> and <i>Pa/SiO<sub>2</sub></i> -CB slurries with irradiation time a) 600s, b) 3000s, and c) 3600s.	37
Figure 3.12: Thermal storage capacity of base fluid and the slurries containing different PCM for heights a) $y/H=0.05$ , b) $y/H = 0.44$ , c) $y/H = 1$ .	39
Figure 3.13: Efficiencies during phase change at different heights (represented in the bottom x-axis) and the corresponding phase change time (represented in the top x-axis), for a) pure <i>PA/SiO<sub>2</sub></i> , b) <i>PA/SiO<sub>2</sub></i> 2wt%-9PPMCB slurry, and c) <i>PA/SiO<sub>2</sub></i> 4wt%-18PPMCB slurry; in comparison with water.	40
Figure A1.1 :Installed solar simulator without beam concentrator.	47
Figure A1.2: Solar simulator with beam concentrator.	47

Figure A1.3: Spectral distribution of AM1.5G simulators normalized to ASTM E892 standard spectrum [44].	48
Figure A1.4: Spectral irradiance of 450W xenon bulbs [43].	48
Figure A1.5: Installed 450W xenon ozone free lamp with heat sink.	48
Figure A1.6: Spectral match of Sol3A solar simulator [42].	49
Figure A1.7: Non-uniformity of sol3A simulator[42].	49
Figure A2.1: Transmission of light through uncoated UV fused silica window.	51
Figure A2.2: Quartz window.	51
Figure A2.3: Isometric view of the collector.	52
Figure A2.4: 3D printed collector.	52
Figure A2.5: Collector holder design.	52
Figure A2.6: 3D printed collector holder with collector and insulation.	52
Figure A2.7: DAQ system with transmitters.	53
Figure A2.8: Solar simulator intensity measurement set up.	53
Figure A2.9: RTD calibration set up.	54
Figure A2.10: RTD calibration at 0°C.	54
Figure A2.11: Measured voltage standard deviation of 3 trials for all the RTD used in the photothermal experiment. Maximum standard deviation is within 3.5%.	54
Figure A2.12: Temperature as a function of voltage for all the 8 RTD.	54
Figure A3.1: SEM image of palmitic acid.	55
Figure A3.2: DSC of palmitic acid.	55
Figure A3.3: Transmittance spectra of water, palmitic acid and photothermal slurry.	55

## List of Tables

Table 2.1: Physical and thermal properties of the working fluid.	21
Table 3.1: Average temperature summary after 9000s.	26
Table 3.2: Summary of temperature variation compared to water at top and bottom of the collector for different time.	30
Table 3.3: Optimum collector height for PA/SiO <sub>2</sub> -CB slurries based on temperature increment compared to water.	31
Table 3.4: Efficiency compared to water at top and bottom of the collector for different time.	35
Table 3.5: Efficiency comparison for all the fluids up to 1 hour at different height.	37
Table A1.1: Performance and technical specifications of the solar simulator.	47
Table A1.2: Percentage change in non-uniformity with partial sun attenuator installed on sol3A solar simulator [42].	50
Table A2.1: Specifications of quartz window.	51
Table A2.2: Specifications of Collector.	52
Table A2.3: Specifications of RTD Pt-100.	53

# Nomenclature

## Abbreviations

DASC	Direct absorption solar collector
HTF	Heat transfer fluid
LFTF	Latent functional thermal fluid
PCM	Phase change material
SWCNH	Single wall carbon nanohorns

## Subscripts

$bf$	Base fluid
$Coll$	Collector
$nf$	Nanofluid
$np$	Nanoparticle
$PCM$	Phase change material
$wf$	Working fluid
$A_{Coll}$	Surface area of the receiver [ $m^2$ ]
$C$	Solar concentration factor
$(C_p)_{bf}$	Specific heat of the base fluid [ $J kg^{-1}K^{-1}$ ]
$(C_p)_{nf}$	Specific heat of the nano fluid [ $J kg^{-1}K^{-1}$ ]
$(C_p)_{np}$	Specific heat of the nanoparticle [ $J kg^{-1}K^{-1}$ ]
$(C_p)_{wf}$	Specific heat of the working fluid [ $J kg^{-1}K^{-1}$ ]
$(C_p)_{PCM}$	Specific heat of the phase change material [ $J kg^{-1}K^{-1}$ ]
$(C_p)_{shell}$	Specific heat of the shell [ $J kg^{-1}K^{-1}$ ]
$(C_p)_{slurries}$	Specific heat of the photothermal slurries [ $J kg^{-1}K^{-1}$ ]
$G$	Irradiance of the solar simulator [ $Wm^{-2}$ ]
$\Delta H_m$	Latent heat of fusion [ $J kg^{-1}$ ]
$m_{PCM}(y)$	Mass of the PCM [ $kg$ ]
$m_{wf}$	Mass of the working fluid [ $kg$ ]
$m_{wf}(y)$	Mass of the working fluid at a given height [ $kg$ ]
$Q_I$	Total incident energy on the collector [ $J$ ]
$(Q_{absorbed})_{wf}$	Heat absorbed by the working fluid [ $J$ ]
$(Q_{absorbed})_{wf}(y)$	Heat absorbed by the working fluid as a function of collector height [ $J$ ]
$Q_{latent}(y)$	Latent heat [ $J$ ]
$t$	Total amount of time exposed to solar radiation [ $s$ ]
$T_{bulk}$	Average bulk temperature of the working fluid [ $K$ ]
$T_{in}$	Average initial temperature of the working fluid [ $K$ ]
$T_{(bulk)}(y)$	Average bulk temperature as a function of height [ $K$ ]
$V_{wf}(y)$	Volume of the working fluid as a function of collector height [ $m^3$ ]
$y$	Collector height as a function of thermometer location in the collector [ $m$ ]
$\rho_{bf}$	Density of base fluid [ $kg m^{-3}$ ]
$\rho_{nf}$	Density of nano fluid [ $kg m^{-3}$ ]
$\rho_{np}$	Density of the nanoparticle [ $kg m^{-3}$ ]
$\rho_{PCM}$	Density of the phase change material [ $kg m^{-3}$ ]
$\rho_{shell}$	Density of the shell around PCM [ $kg m^{-3}$ ]
$\rho_{slurries}$	Density of the photothermal slurries [ $kg m^{-3}$ ]
$\rho_{wf}$	Density of the working fluid [ $kg m^{-3}$ ]
$\phi_{np}$	Volume fraction of the nanoparticle.

$\phi_{PCM}$	Volume fraction of the phase change material
$\phi_{shell}$	Volume fraction of the shell material for the PCM
$\eta_{Collector}$	Efficiency of the collector.



# Chapter 1

## Introduction

### 1.1 Background

Energy is the most fundamental and essential part of everyday life. It plays a prominent role in the development of civilization and is a major issue in politics and diplomacy around the world [1]. With the unprecedented increase in the demand for energy, the gap between the demand and supply is further increasing [2]. According to a statistical review of world energy, the global primary energy consumption comprising of commercially traded fuels, including renewables used to generate electricity, increased from 1.2% in 2016 to 2.2% in the year 2017 [3]. It is expected that the total primary energy demand continues to rise to 26% by the year 2040, based on the current increasing trend and implemented energy policies [4]. Currently, to meet the demand, non-renewable sources of energy such as fossil fuels, oil, natural gases are used which are not sustainable and the cause for global warming [5].

Over the last two centuries, there has been a huge investment and development in the energy infrastructure for coal, oil power plants, so that there is abundant energy to meet the modern energy demands of the fast-growing human population. As a consequence, the amount of naturally generated thermal energy has increased on the earth surface damaging the environment and affecting the climate drastically [5].

With the advent of fossil fuels and rapid growth of new energy infrastructure based on the abundant use of fossils, has been the cause for the decrease in the research and development of solar energy utilization. In an attempt to reduce the dependence on fossil fuels, there are tremendous research carried out in the past few decades, to utilize renewable energy and develop sustainable energy conservation techniques [5][6]. This is one of the most important challenges facing society today [7]. On the positive side, the share of renewable in global power generation increased from 7.4% to 8.4% in 2017, this is 17% higher than the 10-year average and the largest increment on record [3].

Among the alternative sources of energies available to replace fossil fuels, solar energy stands out because of its long history with humankind, inexhaustible, carbon-neutral, least environmental impact, readily available, minimum or no requirement of transportation and free availability for every human being all over the world. Also, solar energy is directly or indirectly origin of many other renewable sources such as wind, biomass, hydro [8][9][10][11][12].

According to an estimation, the amount of solar radiation received was about 174PW at the upper atmosphere, around 49% is lost due to attenuation by atmosphere and clouds, remaining 51% reaches the land and oceans, as shown in figure 1.1. Despite this attenuation, hourly solar flux on earth's surface is far greater than all of the human energy consumption annually [13][14][15][2]. The primary problem lies in effectively collecting, converting this energy into more useable energy forms such as heat and electricity. The next major problem in solar thermal energy utilization is that solar energy is intermittent [16]. To overcome this drawback thermal energy storage is proposed because it can store solar thermal energy and correct the mismatch between the supply and demand of energy [6], this is further elaborated in the following section.

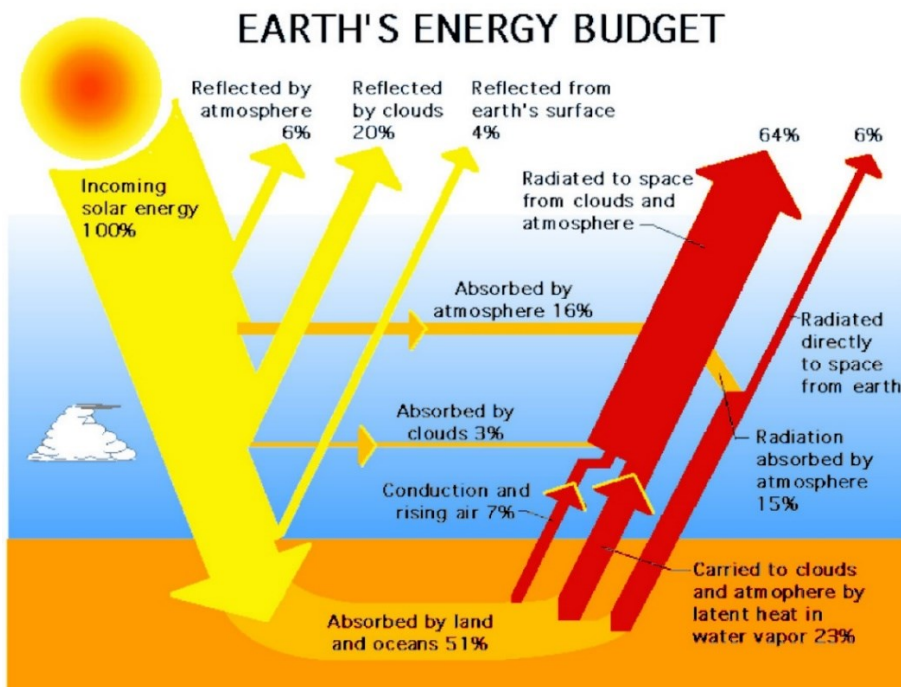


Figure 1.1: Solar energy availability[18].

Focusing on the primary problem, there are different energy conversion principles available to convert solar energy to other useful forms. The most common solar energy conversion methods include thermal, electric and chemical [10]. The common applications of these conversion methods respectively are concentrated solar power, solar photovoltaic cells and photochemical synthesis [5][17]. To flourish the solar energy harvesting technologies, for heating and cooling applications of industrial, commercial, residential, and service sector, the significant technological improvement must be achieved and importance must be given to lowering the cost and increasing the efficiency [2][18].

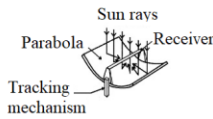
In the conventional solar thermal energy systems, energy from the sun rays is collected by the solar thermal collectors like plates or tubes coated with a layer of selectively absorbing material. The absorbed energy is transferred to the heat transfer fluids (HTFs) driven by a temperature difference [17], which is then either converted to electrical energy or directly utilized as heat energy. Therefore, the efficiency of such a system is largely dependent on the collector efficiency.

The solar thermal collector is an important part of solar thermal utilization system, a device for collecting and converting solar radiation into heat energy [19]. There are a wide variety of solar thermal collectors available. Depending on the available level of solar radiation, a range of fluid working temperatures can be achieved. For simple unglazed swimming pool collectors it can reach up to 50°C, with glazed flat plate collectors can go up to 85°C, and evacuated tube collectors are used to reaching up to 120°C. To achieve further higher temperature, systems involve concentrating the sunlight onto a highly absorptive receiver. The most common in this category of high-temperature solar collectors include parabolic troughs that can reach 400 °C, and for even higher temperatures dish concentrators are employed [20]. In general, solar thermal collectors can be classified into two categories, as highlighted in the figure below:

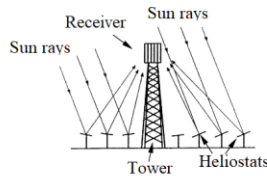
Concentrating type, this include parabolic trough, heliostat, and parabolic dish; and non-concentrating type, like flat plate collectors, evacuated tube collectors and direct absorption solar collector (DASC) [2].

### Concentrating Solar Thermal Collectors

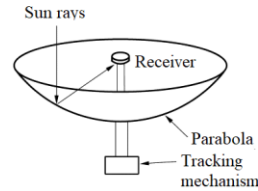
#### Parabolic Trough



#### Heliostat

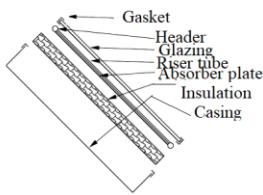


#### Parabolic Dish

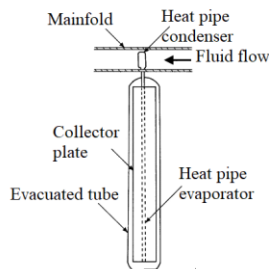


### Non-Concentrating Solar Thermal Collectors

#### Flat Plate Solar collector



#### Evacuated Tube Collector



#### Direct Absorption Solar Collector

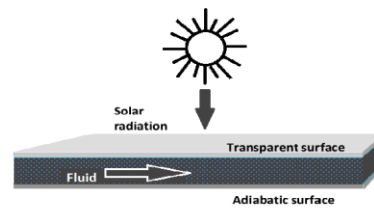


Figure 1.2: Solar thermal collectors general classification [21].

This thesis will be focusing on the non-concentrating types of solar thermal collector, mainly DASC. In the following section, the advantages and limitation of this system will be explained.

## 1.2 Non-concentrating solar thermal collectors

The commonly used non-concentrating solar thermal collectors are shown in figure 1.2. The general outline on the working principle, merits and demerits are discussed below.

- 1) Flat plate solar collector: In this type of solar thermal devices, a black surface is used as the solar absorber. The absorbed heat is transferred by conduction and convection to the heat transfer fluid (HTFs) running in tubes embedded within or fused onto the surface. Since the heat has to be absorbed by one medium and then transferred to another medium (i.e., from the black absorber to the heat transfer fluid), there are high heat losses between the mediums and also with the surrounding. Therefore, the overall efficiency of the solar to thermal energy conversion is limited[11][17][21]. To overcome the limitation of poor thermal efficiency, corrosion and heating losses, a different design of collector called direct volumetric receivers or DASC is proposed [11][22], as explained below.
- 2) Direct absorption solar collector (DASC): The concept of DASC was initially proposed in 1970 by Minardi and Chuang. In this type of collector, the solar energy is directly absorbed within the heat transfer fluid volume instead of the solid coatings and it is converted to thermal energy [23]. Since it reduces the radiant heat transfer losses and avoids the temperature difference between the absorbing material and the heat transfer fluids (HTFs), it has higher outlet temperature and collector efficiency, compared to the conventional solar collector[11][15][22]. Besides, eliminating the use of metal

absorbers decreases the possibility of corrosion [21]. The important parameters that limit the direct volumetric receivers efficiency and overall system performance are optical absorption, thermo-physical properties and photo-thermal conversion performance of heat transfer fluids, hence it is crucial to develop a novel HTFs [9][11].

Heat transfer fluids are used as the medium for energy conservation and heat transfer. The commonly used HTFs are water, ethylene glycol, thermal oil, and ionic liquids. The limitations of these traditional HTFs are its low thermal conductivity; low absorption properties in the visible spectrum, which contains 44% of the solar radiation energy [11][7]; and conversion losses, which results in the reduction of solar collector efficiency [1].

To overcome the drawback of low absorptivity, micro-sized particles were added to HTFs. For low flux collectors, India ink was seeded into the base fluid, a suspension of micron-sized carbonaceous particles. For high flux collectors, micron-sized are suspended in falling films or seeded in a high-velocity gas stream [7][23]. But this didn't solve the problems like particles settling out of solution, clogging of pumps and valves, fouling of transparent tubing and absorption spectrum dominated by the bulk material properties. With recent advancement in thermal engineering, these limitations have been overcome with the dispersion of nanoparticles into the traditional HTFs, known as nanofluids [24]. This is further discussed in the following sections.

### 1.3 Nanofluids

Nanofluid is an advanced kind of heat transfer fluids that contains nanoparticles of a higher degree of thermal conductivity dispersed in a continuous liquid phase. This helps to increase the heat transfer coefficient of the liquid phase/ base fluids/ traditional HTFs for a rapidly increasing number of solar energy harvesting applications [5]. The recent development in nanotechnology has caught researchers interest in radiative properties of nanoparticles in liquid suspensions. This is due to the tunability of the absorption spectrum and improvement in the optical properties of the system [7]. The other benefits of using nanofluids are that the base fluid simultaneously exhibits the superior thermal conductivity of the solid nanoparticles and the excellent fluidity characteristics of the traditional HTFs [25]. Nanofluids are prepared by dispersing uniform nanosized materials into the conventional heat transfer fluids (HTFs). The dispersed nanosized materials can be composed of metal, metal oxide and carbon. Carbon nanomaterials have a positive outlook for use in DASC, due to their black color and high thermal conductivity [9]. This improved thermal and heat transfer characteristics of nanofluids find application in the heating of buildings and reduction of pollution [26], solar energy systems [22], thermal storage, vehicle thermal management, space & military systems, medical applications and nuclear reactors [27].

The use of nanofluids enables to deliver the same amount of thermal energy with a lesser quantity of HTFs as compared to the use of only base fluids requiring larger heating system, thus the nanofluid system requires less power to operate and less material waste to discard at the end of its life cycle hence reducing environmental pollution [26]; The use of nanoparticles ensures greater specific surface area, this provides more heat transfer surface between particles and the fluids [27]; Depending on the need of applications the nanofluid properties such as thermal conductivity, can be adjusted by varying the particle concentration [27]. Nanoparticles have much larger absorption efficiency compared to scattering efficiency [7]. On the other

hand, the factors hindering the further development and applications of nanofluids are long term stability, increased pumping power, thermal performance in turbulent flow, lower specific heat of nanofluids and higher production cost [27].

There are numerous experimental research in the past decade to support the idea of using nanofluids in DASCs; summary of them are outlined. In the primary research, Sani et al [28] investigated single-wall carbon nanohorns (SWCNHs) in an aqueous medium for different nanoparticle concentration, the results showed SWCNHs improved the thermal conductivity by 10% and photonic properties of the fluid at very low nanoparticle concentration. In their continued research [29], SWCNHs and carbon black were dispersed in ethylene glycol and same properties were studied; SWCNHs-glycol nanofluid showed better optical absorption properties and more stability in a stationary condition, increasing its reliability as direct absorbers in solar devices. Otanicar et al [7], reported their experimental findings of carbon nanotubes, graphite and silver nanoparticles, of different sizes, dispersed in de-ionized water; 30nm graphite and 20nm silver nanoparticle showed a maximum efficiency improvement of 3% and 5% respectively, with the volume fraction of nanoparticles up to 0.5%. The other problem of low specific heat of the working fluids used in DASC can be improved by adding phase change materials (PCMs), this is further discussed as follows.

#### **1.4 Phase change material (PCM) slurries**

Phase change materials are special kind of material, in addition to sensible heat, it also possesses latent heat in the process of melting and solidifying [30]. These materials provide high thermal storage density without a drastic rise in temperature [31][32]. Using this concept, PCMs can store solar thermal energy and corrects the mismatch between supply and demand of energy[11], thereby tackling the problem of solar energy intermittence.

There are a different classification of the PCMs, solid-liquid phase transition PCMs account for the substantial part. Among the solid-liquid PCMs, organic PCMs are considered favorable due to good chemical stability, no phase segregation during the repeated phase change process, nearly no supercooling, low vapor pressure and non-corrosiveness [33]. On the downside problems like leakage, non-effective use of solar radiation and high changes in volume on phase change restricts their direct application [6].

To overcome the above-mentioned problem of leakage, the microencapsulation technique is used. In this technique, a robust shell around the PCMs is developed. This helps to increase the heat transfer area, control volume changes during the phase transition and reduce PCMs reactivity towards the outside environment. The shell can be made from organic or inorganic materials. Polymers like polymelamine-formaldehyde (PMF) resin, polyurea-formaldehyde (PUF) resin, polyurea (PU), polystyrene (PS) and polymethyl methacrylate (PMMA) are commonly used as the shell material [11]. That is due to the outstanding sealing tightness, low price, thermal stability, appropriate plasticity and chemical resistance [6]. The conventional heat transfer fluids (HTFs) can be incorporated with microencapsulated PCMs to prepare latent functional thermal fluid (LFTFs). The LFTFs enhances the heat transfer by increasing the apparent specific heat of the HTFs.

Furthermore, to solve the problem of not being able to effectively absorb and transfer solar energy to heat energy, photothermal conversion PCMs are being researched. Photothermal

PCMs possess the ability to harvest sunlight by the introduction of the nanomaterials with effective photon capturing ability such as dyes, graphite foam, expanded graphite, graphene oxide, carbon nanotube, graphene aerogels, graphene nanosheet and so on [6]. This modified latent functional thermal slurries with nanoparticles exhibit enhanced thermal conductivity and high specific heat. The followings are the research results supporting the idea of photothermal PCMs: Chen[34] studied the thermal properties of graphene oxide modified poly(melamine-formaldehyde) microcapsules containing n-dodecanol as the phase change material; the results were favoring the graphene oxide modified micro-PCM slurry.

Wang et al. [35] prepared a double-walled shell: polystyrene as interior shell and graphene oxide as the exterior shell, with n-hexadecane as the core PCM, the results showed outstanding thermal stability and protected the core PCM from leakage and evaporation, because of good barrier properties of graphene oxide.

Fang et al. [9] studied paraffin as the core and the MF resin as the shell, with graphite nanoparticle modifying the micro-PCM, dispersed into an ionic liquid. At a given concentration, micro-PCM modified with graphite nanoparticle slurries exhibited high photothermal performance and thermal conductivity compared with micro-PCM slurries, showing a great potential to be used as medium-temperature heat transfer fluids.

Based on the above research, one can predict the micro-PCM modified with carbon nanoparticles slurries, exhibit enhanced thermal conductivity and high specific heat, making them very promising working fluids for DASC's.

## 1.5 Research goals

Despite numerous research on thermal properties of microencapsulated phase change materials modified with nanoparticles, there is limited research on the photo-thermal performance of these slurries in DASC systems. To have a better understanding of the advantages, disadvantages and overall performance of PCM slurries with modified nanoparticles in DASC systems, the following aspects of this system are researched:

1. Design and installation of the simulated lab-scale stationary state condition in DASCs.
2. Investigation of the photo-thermal performance of slurries including both sensible and latent heat storage.
3. Studying the effect of different parameters including collector height, irradiation time, and the existence of thermal storage on the collector efficiency, leading to the optimized collector.

## 1.6 Outline of the thesis

This thesis consists of four chapters. The first chapter gives an introduction about the solar collector technologies, literature review of DASC and presents the research goals. Chapter 2 discusses the working principle, experimental setup, the design of the set-up, calibration of the set-up, the used working fluids and the experimental procedure. Chapter 3 discusses the obtained results of the experiment. Finally, Chapter 4 delivers conclusions and recommendations for future work.

## Chapter 2

### Methodology

This chapter presents the working conception of the photo-thermal slurry in DASC. The design procedure and installation of the stationary state DASC experimental setup are explained, in the following section. Then the solar simulator and temperature measurement devices calibration are discussed. Next, the working fluid properties are studied. And finally, the procedures implemented to perform the photo-thermal experiments are described.

#### 2.1 Working concept/ theory

The idea behind the direct absorption solar collector is to directly absorb the incident solar radiation volumetrically by the working fluid, and convert this incident radiation to heat energy. For effective absorption and improved efficiency of the DASC system, the design of the collector and the constituents of the heat transfer medium have a significant role. In this thesis, the following activities are done:

- The collector is used to hold the sample and designed to minimize the heat losses by convection and radiation to the surrounding.
- Carbon nanoparticles are added to increase the thermo-physical properties of the heat transfer fluid.
- Along with nanoparticles, phase change materials (PCMs) are added to improve the specific heat and act as the thermal storage medium. This is schematically shown in figure 2.1.

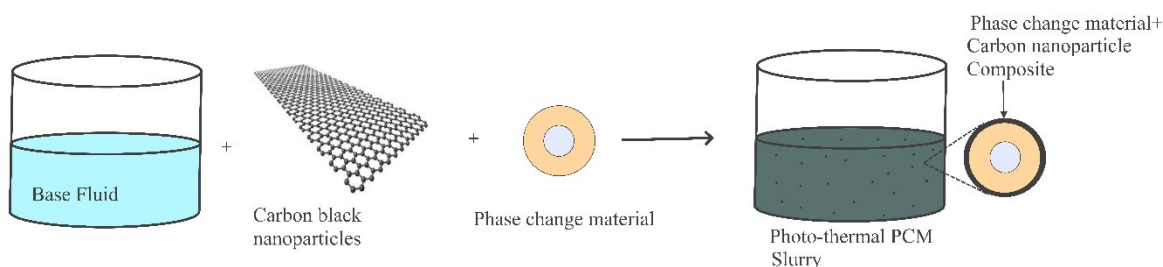


Figure 2.1: Concept of photothermal slurries.

For the static analysis of the DASC system, the nanofluid with PCM is enclosed in an adiabatic cylindrical container, with the top of the container covered by a transparent window. The transparent window allows the incident solar heat flux to be transmitted vertically and is absorbed in volume by the suspended nanoparticles, because of their superior absorptive properties compared to base fluid and the PCM's. Some fraction of the incident radiation is absorbed by nanoparticle and is transferred by conduction to the PCM's, this further simultaneously heats the base fluid. The remaining fraction of the incident radiation is being transmitted to the next layer, increasing the overall temperature of the working fluid. During propagation in the working medium, incident radiation is also reflected and scattered. The bottom and sidewalls of the collector are considered to be adiabatic and highly opaque. The receiver heat losses are assumed to be due to convection at the top surface, as it is exposed to

the ambient atmosphere and thermal re-emission from the suspended particles. This is diagrammatically shown in figure 2.2.

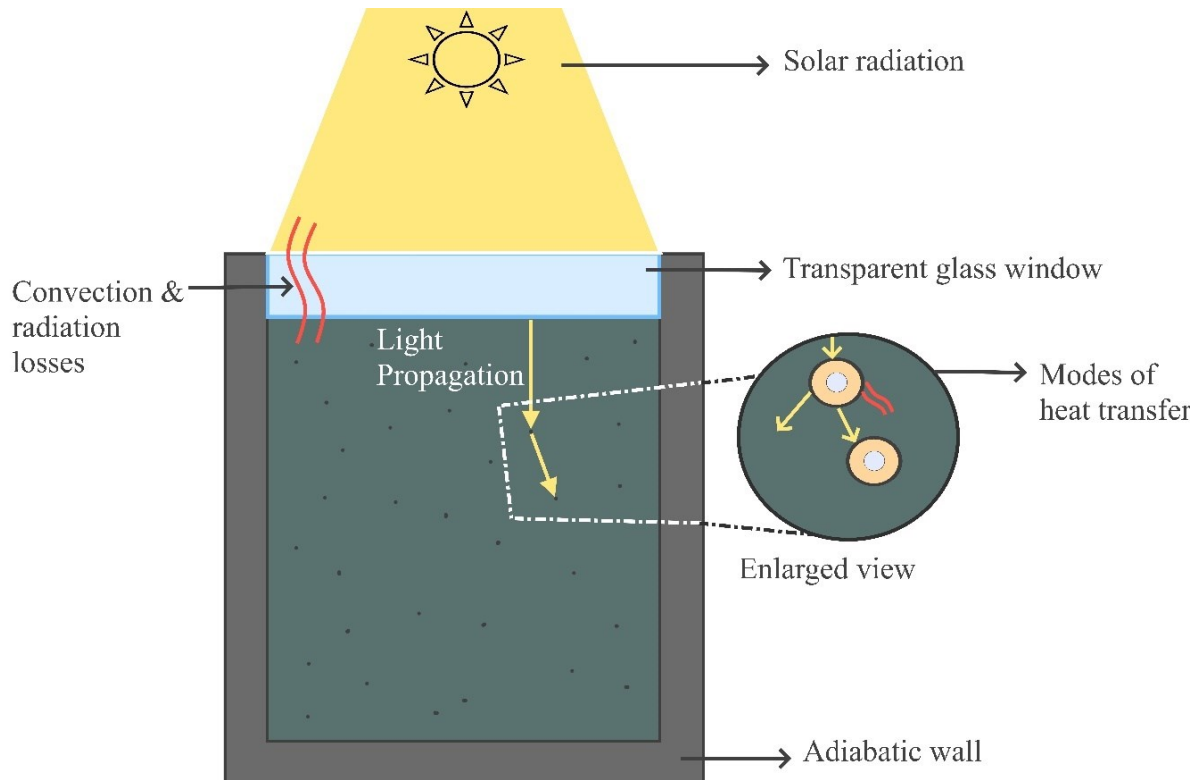


Figure 2.2: The working concept of photothermal slurries in DASC.

In the experiments, the solar simulator is used to artificially produce solar heat flux in the UV-visible light spectrum. Therefore, the total incident energy on the collector ( $Q_I$ ) is proportional to the solar simulator light intensity, the collector area on which simulated light is incident and a total time of irradiation and is given by equation Eq 2.1.

$$Q_I = C \cdot G \cdot A_{Coll} \cdot t \quad \text{Eq 2.1}$$

Where:

$C$  is the concentration factor

$G$  is the irradiance of the solar simulator in  $\frac{W}{m^2}$

$t$  is the total irradiation time in *second(s)*

$A_{Coll}$  is the surface area of the receiver in  $m^2$ , given as  $A_{Coll} = \frac{\pi}{4} \cdot (D_{Coll})^2$ .

$D_{Coll}$  represents the diameter of the collector in meter (m), it is determined to be 30 mm and from this the area is calculated to be  $706.85mm^2(706.85 \times 10^{-6}m^2)$ .

The heat absorbed by working fluid ( $Q_{absorbed}$ )<sub>wf</sub> depends on the specific heat capacity of the fluid, the mass of the fluid and the change in the temperature during the illumination represented by the equation 2.2. And the overall collector efficiency ( $\eta_{Collector}$ ) is the ratio of the heat absorbed by the working fluid to the incident radiation and is given by expression Eq 2.3.

$$(Q_{absorbed})_{wf} = m_{wf} \cdot (C_p)_{wf} \cdot (T_{bulk} - T_{in}) \quad \text{Eq 2.2}$$

$$\eta_{Collector} = \frac{(Q_{absorbed})_{wf}}{Q_I} = \frac{m_{wf} \cdot (C_p)_{wf} \cdot (T_{bulk} - T_{in})}{C \cdot G \cdot A_{Coll} \cdot t} \quad \text{Eq 2.3}$$

Where:

$m_{wf}$  is the mass of the working fluid in  $kg$

$(C_p)_{wf}$  is the specific heat of working fluid in  $J/kgK$

$T_{bulk}$  is the average temperature of the fluid inside the collector at a particular instant of time in  $K$

$T_{in}$  is the average initial temperature of the fluid in the collector in  $K$ .

The absorbed energy and collector efficiency at different heights of the receiver are given by the equation Eq 2.4 and equation 2.7 respectively. The absorbed energy at a particular height varies as a function of the mass and temperature change corresponding to the same height.

$$(Q_{absorbed})_{wf}(y) = m_{wf}(y) \cdot (C_p)_{wf} \cdot (T_{(bulk)}(y) - T_{in}) \quad \text{Eq 2.4}$$

$$m_{wf}(y) = \rho_{wf} \cdot V_{wf}(y) \quad \text{Eq 2.5}$$

$$V_{wf}(y) = \frac{\pi}{4} \cdot (D_{Coll})^2 \cdot y \quad \text{Eq 2.6}$$

$$\eta_{Collector}(y) = \frac{(Q_{absorbed})_{wf}(y)}{Q_I} = \frac{m_{wf}(y) \cdot (C_p)_{wf} \cdot (T_{(bulk)}(y) - T_{in})}{C \cdot G \cdot A_{Coll} \cdot t} \quad \text{Eq 2.7}$$

Where:

$y$  represents the different collector height in meter(m)

$\rho_{wf}$  is the density of the working fluid in  $\frac{kg}{m^3}$  (determined theoretically as explained below)

$V_{wf}(y)$  is the volume of the collector at a given height in  $m^3$

$T_{(bulk)}(y)$  is the average bulk temperature at a particular height of the collector at the given instant of time.

In the experiments different working fluids like base fluid, nanofluid and PCM-nanofluid are irradiated under the simulator. Depending on the type of working fluid used in the experiment, the value of  $\rho_{wf}$  and  $(C_p)_{wf}$  changes in the above equations, and is determined as follows. If the working fluid is only base fluid( $bf$ ), then  $\rho_{bf} = 1000 \frac{kg}{m^3}$  and  $(C_p)_{bf} = 4.184 \text{ kJ/kgK}$ .

If the working fluid is nanofluid (base fluid + nanoparticles), then the following expression holds:

$$\rho_{wf} = \rho_{nf} = ((1 - \phi_{np}) \cdot \rho_{bf}) + (\phi_{np} \cdot \rho_{np}) \quad \text{Eq 2.8}$$

$$(C_p)_{wf} = (C_p)_{nf} = ((1 - \phi_{np}) \cdot (C_p)_{bf}) + (\phi_{np} \cdot (C_p)_{np}) \quad \text{Eq 2.9}$$

Where subscript  $nf$  represents nanofluid,  $\phi_{np}$  is the volume fraction of the nanoparticle in percentage,  $\rho_{np}$  is the density of nanoparticle,  $(C_p)_{np}$  is the specific heat capacity of the

nanoparticle,  $w$  is the mass fraction and subscript  $bf$  and  $np$  represents for the base fluid and the nanoparticles respectively, and other terms have the same meaning as described above.

If the working fluid is photothermal PCM slurries, then the equations are

$$\rho_{wf} = \rho_{slurries} \quad \text{Eq 2.10}$$

$$= ((1 - \phi_{np} - \phi_{PCM} - \phi_{shell}) \cdot \rho_{bf}) + (\phi_{np} \cdot \rho_{np}) \\ + (\phi_{PCM} \cdot \rho_{PCM}) + (\phi_{shell} \cdot \rho_{shell})$$

$$(C_p)_{wf} = (C_p)_{slurries} \quad \text{Eq 2.11}$$

$$= ((1 - \phi_{np} - \phi_{PCM} - \phi_{shell}) \cdot (C_p)_{bf}) + (\phi_{np} \cdot (C_p)_{np}) \\ + (\phi_{PCM} \cdot (C_p)_{PCM}) + (\phi_{shell} \cdot (C_p)_{shell})$$

Where subscript *slurries* represent photothermal PCM slurries, subscript *PCM* represents the corresponding properties of PCM, and other terms have their usual representation as indicated above.

During the phase change process, the additional heat absorbed by the photothermal slurry is used for the phase transition from solid PCM to liquid PCM. The latent heat stored during the phase change depends on the effective mass of the PCM and the latent heat of fusion. This is represented by Eq 2.12.

The latent heat is added to Eq 2.7 to determine the overall performance of the collector during the phase change process and is as shown in Eq 2.13.

$$Q_{latent}(y) = m_{PCM}(y) \cdot \Delta H_m \quad \text{Eq 2.12}$$

$$\eta_{Collector}(y) = \frac{(Q_{absorbed})_{wf}(y) + Q_{latent}(y)}{Q_I} \quad \text{Eq 2.13}$$

$$= \frac{m_{wf}(y) \cdot (C_p)_{wf} \cdot (T_{(bulk)}(y) - T_{in}) + m_{PCM}(y) \cdot \Delta H_m}{C \cdot G \cdot A_{Coll} \cdot t}$$

Where:

$m_{PCM}(y)$  is the mass of PCM at a given height in  $kg$

$\Delta H_m$  is the latent heat of fusion of the PCM in  $\frac{J}{kg}$

To check the photothermal performance of the working fluid, the conceptual idea has to be translated into an experimental setup, this is further discussed in the following section.

## 2.2 Experimental setup

To evaluate the photothermal conversion performance of the different working fluids for the direct absorption solar collector, a lab-scale stationary state experimental setup have been designed and installed, as illustrated in the figure 2.3. The experimental setup can be divided into two components: the photothermal conversion system and data collection system, as shown in figure 2.3.

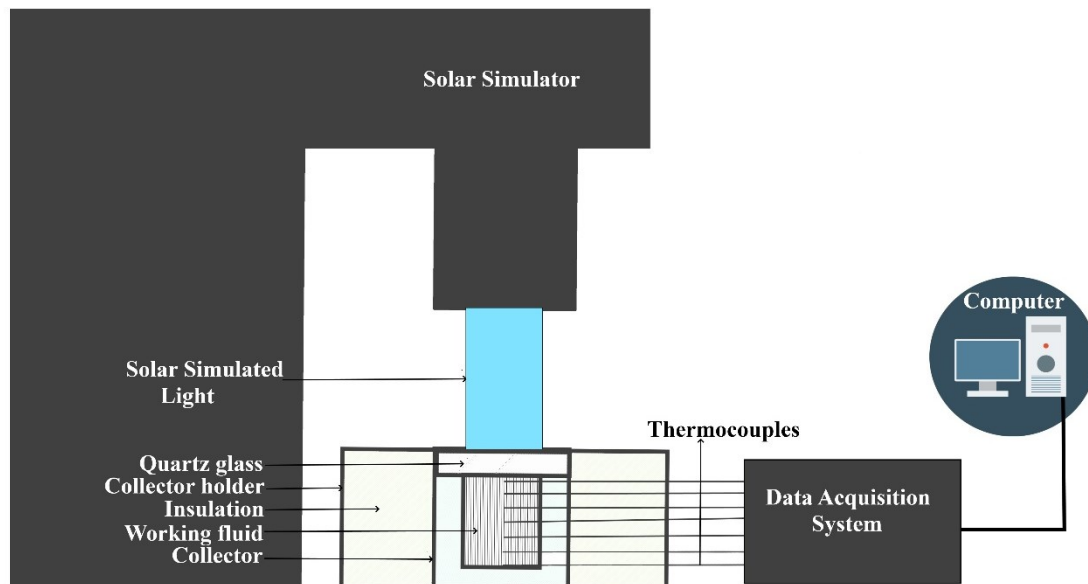


Figure 2.3: Schematic of Direct Absorption Solar Collector experimental setup.

The photothermal conversion system consists of the solar simulator, collector, collector holder with insulation, and quartz window. The data collection system consists of thermocouples, data acquisition system, and the computer. The design of the solar collector system and instrumentation details are further discussed from sections 2.2.1 to 2.2.7.

### 2.2.1 Solar Simulator

An artificial sunlight simulator, Oriel Sol3A with 450-watt xenon lamp, manufactured by Newport was used as a radiative source for the experiment. The Sol3A simulator is designed to meet class AAA performance for different test requirements like the spectral match, non-uniformity of irradiance, and temporal instability of irradiance. This performance consistency ensures precise and traceable comparison of experimental data. The non-uniformity of irradiance of the system was validated to be 1.60%, as per the IEC standards, this ensures reduced hot spots in the working plane of the output beam. The long and short term temporal instability of irradiance was certified to be 0.47% and 0.10% respectively, ensuring stable light output and minimum fluctuations over time. Thus, the simulator uses a single lamp to meet all three performance criteria, without compromising the 1 Sun output power. The output from the simulator can be measured using a PV reference cell system up to 3.5 suns. The reference cell system consists of a 2x2 cm monocrystalline silicon photovoltaic cell and a type K thermocouple placed in an aluminum housing. The reference meter is calibrated to short-circuit current to read out irradiance from a solar simulator in units of suns. Solar simulator with an

output of  $1000 \frac{W}{m^2}$  with air mass 1.5 global spectral filtering is equivalent to one sun. Further information on the lamp performance criteria is included in Appendix A1.

The installation of the solar simulator includes the following important components [42].

- **An illuminator housing:** The illuminator housing provides a safe enclosure to the optical system, arc lamp, lamp ignitor, cooling system, and other electrical components. Its flat black outer surface minimizes stray light entering the illuminator. The housing is mounted on a riser assembly and this allows the head orientation to produce a downward-facing output beam. The illuminator housing has a control panel, with a switch to power on/off the illuminator, shutter close/ open button and operation indicators. The power on/off switch, powers the illuminator housing and turns on the cooling fans to provide forced-air cooling to maintain optimal lamp, optics, and housing temperature. The shutter close/open switch is used to manually activate the shutter either completely close the simulated light or completely expose the light. The operation indicators include a LED indicator for lamp on, shutter open, lamp replacement and a digital lamp hour indicator for easy monitoring of the lamp usage.
- **Air mass filter:** To match the solar spectrum under varying conditions, air mass(AM) filter is used to correct the arc lamp light output. Sol3A simulator uses an AM1.5G filter, this filter simulates the global solar radiation, when the sun is at a zenith angle equal to  $37^\circ$ , as per the ASTM E 892 standard. It retains the optical properties under the operating conditions without degradation of the filter. The spectral distribution using AM1.5G filter is as shown in the appendix Figure A1.3.
- **Partial sun attenuator:** The partial sun attenuator is designed to manually control the solar simulator irradiance level. The irradiance level can be increased by turning the knob in the clockwise direction and decreased by rotating in the counterclockwise direction. Although using the partial sun attenuator ensures class A spectral match of the system, it affects the uniformity. The percentage change in non-uniformity for sol3A simulator is included in Table A1.2. It is noted that non-uniformity tends to deteriorate, as the irradiance level is decreased.
- **An arc lamp:** The arc lamp produces the sources of light closely matching the UV-VIS solar spectrum. A 450W ozone free xenon short-arc lamp is used for the purpose. The lamp is filled with purified xenon at 5-20 bar and the pressure triples during operation. The radiations are comparable to 5500-6000k black body radiations with some xenon lines superimposition dominant between 750 and 1000nm and the spectrum is shown in the appendix Figure A1.4. It is installed with a heat sink assembly to dissipate the heat produced during the operation of the lamp. The installed lamp is as shown in the appendix Figure A1.5. The power to the lamp is controlled by adjusting the setting in the power supply module.
- **An arc lamp power supply:** The constant electrical power/ current to the 450W xenon lamp is supplied through a high voltage power supply. It helps in maintaining and regulating very stable light output. With the power supply module, it is possible to adjust the output before running the lamp; current, voltage, power and lamp running time can be monitored; Start button controls the ignition of the lamp at preset values; stop button allows to shut down of the lamp. The specifications are included in Table A1.1.

- **High flux beam concentrator:** The high flux beam concentrator focuses the output beam from the simulator, which is 51X51 mm to 30mm diameter spot at a working distance of 57.15mm. The concentrated beam energy density is increased by 9.5 times at 50.8mm working distance from the concentrator, with  $\pm 5\%$  uniformity of intensity. It consists of multi-element fused silica lens assembly in a tube that extends up to 25.4 mm from the base of the solar simulator. The concentrator is attached to the simulator by an adapter that facilitates as a light-tight seal.

The installed solar simulator without and with beam concentrator is shown in the appendix Figure A1.1 and Figure A1.2 respectively.

### 2.2.2 Quartz window

It is a high precision glass window, with UV fused silica as a substrate. The quartz window is placed on top of the collector, it acts as a sealant, insulation to convective losses from the top of the collector and avoids a high evaporation rate. It helps in transmitting the incident solar heat flux from the simulator to the sample held in the collector container. The UV fused silica substrate allows wavelength in the range of 185 nm to 2.1 $\mu$ m. The silica window is 50.8 mm in diameter and 12 mm in thickness. The specifications and transmission data is shown in Appendix A2. The benefits of using this glass window are increased transmission over a wide range of wavelength; for a given wavelength offers a lower index of refraction; better uniformity; and a low coefficient of thermal expansion.

### 2.2.3 Collector

The purpose of the collector in the photothermal conversion system is to hold the working fluid in a stationary state, during the irradiation time. The design requirement considered for the collector are: withstanding operating temperature up to 90°C, the temperature is limited to 90°C because the base fluid is water and hence heating above 90°C leads to evaporation losses and it is not desirable as this affects the concentration of the dispersed particles; low thermal conductivity, to minimize heat transfer losses through the collector walls; and easy machinability, to incorporate 6 thermocouples for temperature measurement at different heights of the collector. Apart from these the top of the collector is closed with the quartz glass and therefore the dimensions should match while they are assembled for experimentation and the working fluid should be within the solar simulator illumination area with and without beam concentrator.

Based on the above criteria collector is designed with the dimensions and other details as shown in the figure 2.4a. The left side of the figure 2.4a shows the dimensions of the collector in mm. The right side of the figure 2.4a shows the cross-sectional view of the collector. The sample is held in the inner cylinder having a diameter of 30mm and height of 30.5mm. Above the inner cylinder, there is a slot of diameter 52.5mm and depth of 8mm to place the quartz window. The inner cylinder wall is separated from the outer cylinder wall by a gap of 3mm, this gap is filled with silicone gel to minimize heat transfer losses from the walls. There is a provision to place thermocouples, indicated by T1 to T6 in figure 2.4a), for determining the temperature distribution of the working fluids. The thermocouple T6 and T5 are separated by 5mm, an equal distance of 6mm is maintained between thermocouples T5-T4, T4-T3, and T3-T2 pair. The last

two thermocouple T2 and T1 are 5.8mm apart so that the first thermocouple is not completely exposed to irradiation and doesn't touch the quartz window. The non-dimensional location of the six thermometers installed in the center of the cylinder is determined to be  $\frac{y}{H} = 0.05, 0.25, 0.44, 0.64, 0.84, 1$ , where 0.05 represents the non-dimensional distance of the first thermometer (T1) from the top of the collector and 1 represents the last thermometer (T6) at the bottom of the collector. Further, the isometric view and dimension specifications of the collector is shown in Figure A2.3 and Table A2.2 in Appendix A2 respectively.

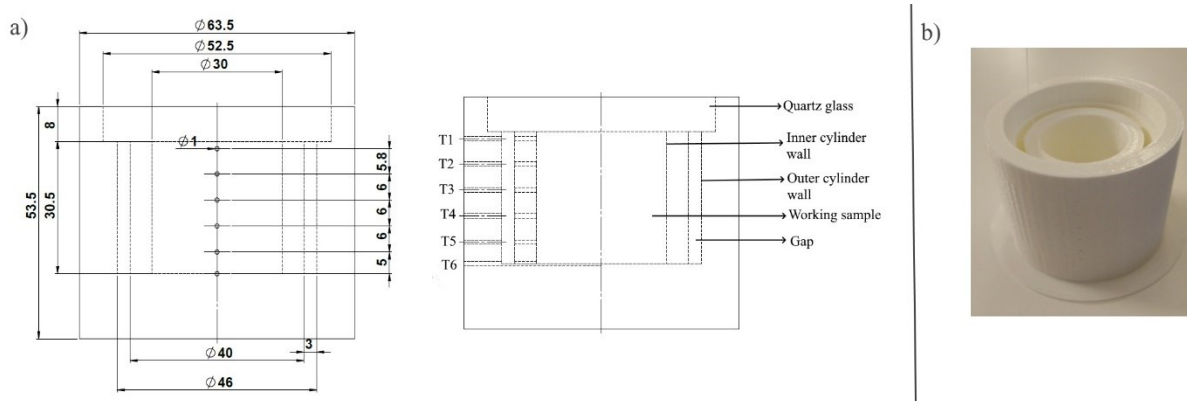


Figure 2.4: a) Dimensions in mm and other details of the collector. b) 3D printed collector.

Next, the modeled design has to be built, for this 3D printing technique is chosen because of its easy prototyping, machinability, and cost. Also, the material used for 3D printing is polylactic acid (PLA) and has a melting point of 145 °C, within the operating limit of 90 °C. The 3D printed collector is as shown in figure 2.4b). To stably hold the collector in place during the experiment, a collector holder is designed and 3D printed, the details are shown in the appendix Figure A2.5 and Figure A2.6. The space in the collector holder is filled with an insulation material made from glass fiber, having a low thermal conductivity of  $0.12 \frac{W}{mK}$  [36]. The insulation minimizes the heat transfer losses and helps to isolate the collector from the surrounding.

The provision for thermocouples is resized, so the thermocouples are tightly held. The thermocouples are placed to the center of the collector. Further to avoid any leakage through the holes made for thermocouples positioning, silicone rubber adhesive is applied in the gap between the inner cylinder wall and outer cylinder wall and also on the periphery of the outer cylinder. This adhesive seals in the operating temperature ranging from -70°C to 200°C and has a low thermal conductivity of  $0.17 \frac{W}{m-K}$ . The flowchart in figure 2.5 highlights the design process followed.

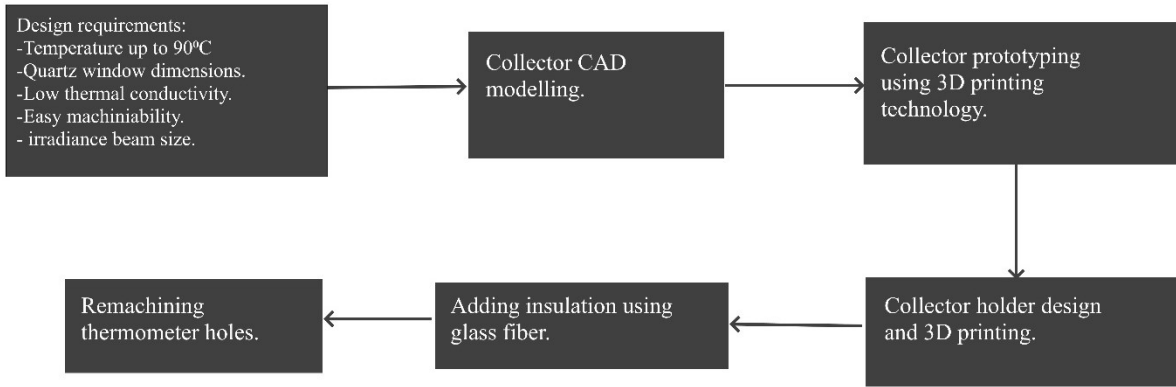


Figure 2.5: The collector design process.

The top of the collector holder is covered with silver reflective tape as shown in Figure A2.6. The purpose of the reflective tape is to minimize the heating of the surrounding materials around the collector, that could influence the sample heating rate. Therefore, the sample in the collector is only heated under the influence of the direct irradiation. The other purpose of the reflective tape is to protect the insulation material from being damped, while transferring the working fluid to and from the collector, before and after the experiment respectively. The installed collector system is as shown in Appendix A2, Figure A2.6.

## 2.2.4 Thermometers

The temperature measurements are performed using a resistance thermometer detectors (RTD's). From the availability of RTD's, PT100 is used for temperature data collection. It works on the principle to measure the resistance of a platinum element. This type of thermometers needs calibration of resistance to a known reference temperature and the relationship between temperature and resistance is approximately linear over a small temperature range. The PT100 from Rossel Messtechnik has an operating temperature range from  $-100^{\circ}\text{C}$  to  $+550^{\circ}\text{C}$  with a tolerance of  $\pm(0.15 + 0.002 * t)$  in  $^{\circ}\text{C}$ , where  $t$  is the operating temperature. The advantage of using this PT100 are: it is highly resistant against vibrations; short response times; mechanically resistant; and easily bendable to a small radius. The other technical specifications are included in Table A2.3. To convert the low-level signal from RTD's into a high-level standard signal, a transmitter is used for this purpose. In the experiment a total of 8 RTD's are used, of which 6 RTD's are used for measuring the temperature of the working sample at different collector heights. The remaining 2 thermometers are used to monitor the surrounding environment temperature.

## 2.2.5 Data Acquisition system (DAQ)

The data acquisition system converts the analog signal into digital values for processing. In the present experiment case, the change in resistance data detected by resistance thermometer is converted to a high-level signal using a transmitter. This high-level signal is detected by the data acquisition device and this device acts as communication between the RTD's and the computer used for logging the data. Based on the calibration, the detected change in resistance is converted to the temperature data using a suitable programming language. The DAQ system

used in the experiment is USB-6009 from National instruments. It is a multifunctional device with analog input/output channels, digital input/output channels and a 32-bit converter with a full-speed USB interface. The USB-6009 is controlled using a graphical programming language LabVIEW with a data collection rate of 2 samples per second. The installed USB-6009 along with transmitter is shown in Figure A2.7.

The installed direct absorption solar collector experimental set up is as shown in the figure 2.6 and 2.7.



Figure 2.6: Data acquisition system.

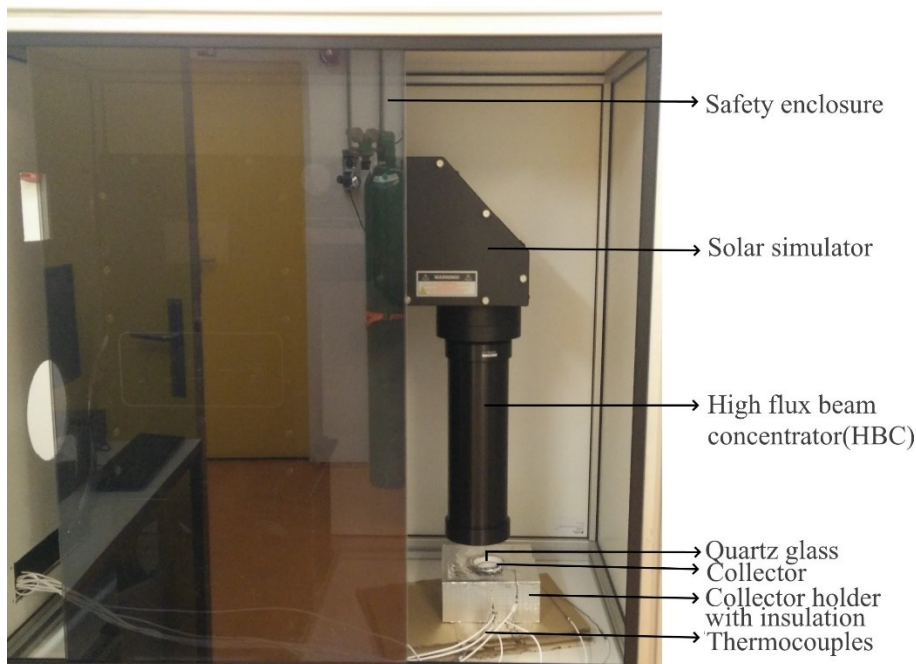


Figure 2.7: Installed solar simulator.

## 2.3 Instrument calibration

### 2.3.1 Solar simulator setup fine-tuning

After installing the 450W lamp in the solar simulator, the solar simulator was tested for different power in the range of +10% to -20% of the nominal lamp rating. This was performed to determine the optimal working power and working distance with good uniformity of spectral intensity close to 1sun in the working plane. The intensity of the illuminator was measured using a PV reference cell at the optical center; at the boundaries of the working plane with coordinates (20,0), (0,-20), (-20,0) and (0,20) mm, with respect to optical center, as illustrated in the figure 2.8 and the actual set up is shown in Figure A2. 8 ; and also at different heights controlled by manually adjusting the lab jack.

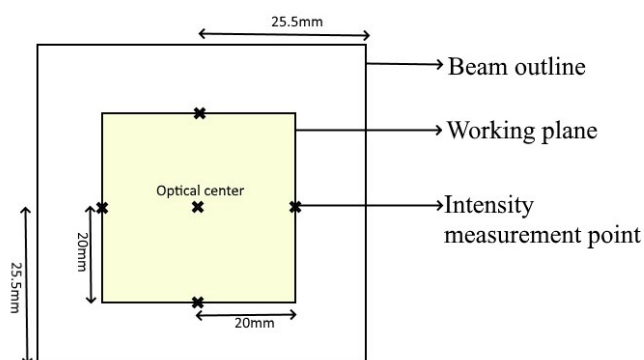


Figure 2.8: Intensity measurement points for the non-uniformity profile.

The photo-thermal experimental sample will be placed within the working plane (40x40mm) and hence the uniformity is checked in this plane rather than the beam profile (51x51mm). At each working plane, the intensity is measured at all the 5 locations. From the known intensities the maximum and minimum are determined, later this is used in the equation A1.1 to determine the percentage non-uniformity in the spectral intensity. This is repeated for different heights and power. The intensity at the optical center as a function of height from the solar simulator to the reference cell, for different power is plotted, in figure 2.9a.

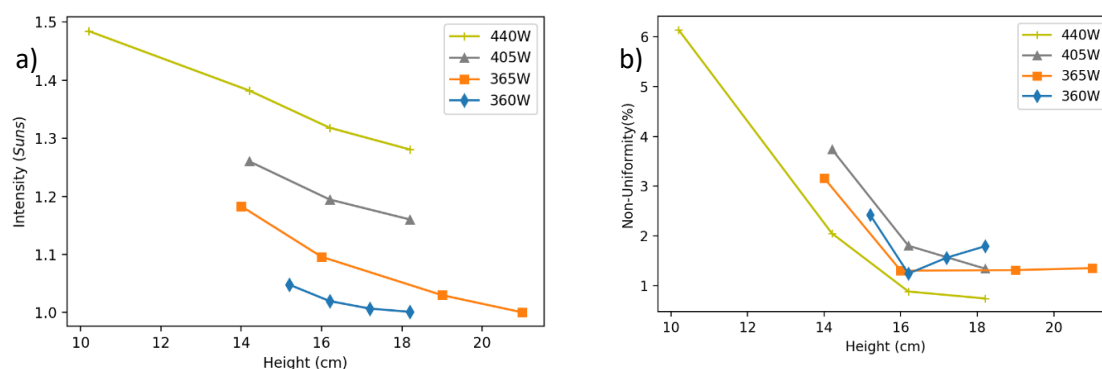


Figure 2.9: a) Intensity (optical center) vs height for different power. b) Non-uniformity as a function of height and power.

To validate the optimal working power and working distance, the percentage non-uniformity vs height for different working power is shown in figure 2.9b. The non-uniformity is almost constant for 365W operating power, in the working distance ranging from 210 to 160 mm. From the previous plot, for operating power of 365W, an initial working distance of 200 mm is chosen with an intensity of 1.01 suns at the optical center.

### 2.3.2 Thermometer calibration

The PT100 thermometers need to be calibrated before starting with the temperature measurements. The calibration process involves relating the detected voltage to a known reference temperature. The melting and boiling point of water is used as the reference temperature. The setup consists of magnetic stirrer with a hot plate from IKA model IKMAG RET, electronic thermometer for temperature regulation from IKA model IKATRON ETS D3, thermometer, glass beaker, demineralized water, 8 RTD's to be calibrated and lab stand with clamps. The purpose of the hot plate with a magnetic stirrer is to maintain uniform distribution of heat in the water, the stirring is controlled by a knob set to the desired rpm. The electronic thermometer that is connected to the hot plate, helps in maintaining the hot plate to the desired temperature and the resolution of the temperature is 1K. The second mercury in glass thermometer is used as a reference thermometer, in addition to the electronic thermometer. To read the voltage output of the RTD's, LabVIEW graphical programming is used. The setup is as shown in Appendix A2, Figure A2.9.

Initially, ice is placed in the glass beaker and it is made sure that all the RTD's and thermometers are in contact with the ice before taking the voltage readings. Next, the hot plate with a magnetic stirrer is turned on, the stirring is set to 700rpm and for every 5 K increase in temperature, the corresponding voltage of the RTD's are noted. It is necessary to make sure the RTD's and thermometers are 70% immersed in the water, during every measurement. This procedure is repeated and from the collected data, the average of the three experimental voltages for different thermocouples is determined at different temperatures.

The plot of temperature versus the averaged voltages for 8 different RTD's is performed, Figure 2.10 shows for one of the RTD labeled T1. To the plotted results a linear curve is fit and its fit curve equation is determined. The closeness of the data points with the fitted curve ( $R^2$  value) is estimated for the plotted results. The  $R^2$  value for all the RTD is determined to be  $\approx 0.9999572$ . The fit curve equation for different PT100 is used in the LabView program to directly relate the detected voltages into temperature.

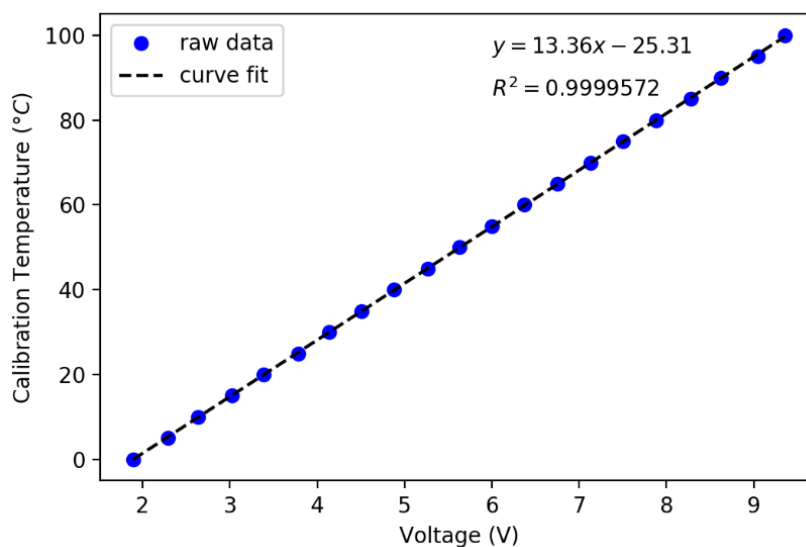


Figure 2.10: Temperature voltage calibration curve.

## 2.4 Working fluids

The working fluids used in this experimentation can be categorized into base fluid, nanofluids, and photothermal slurries. The base fluid is distilled water, and the nanofluids are of two types, graphene nanoplatelet (GNP) and carbon black (CB). The photothermal slurries is a combination of nanofluids and phase change materials. Two different types of photothermal slurries are being tested for efficiency. In one type of slurries, a certain wax is microencapsulated by polyurea shell with GNP, due to confidentiality the results are not presented in this thesis. In the second type of slurries, shape stabilized palmitic acid/ silica dioxide ( $PA/SiO_2$ ) [37] combined with carbon black nanoparticles is studied. The schematic in Figure 2.11 outlines the sample used in the photothermal experiments.

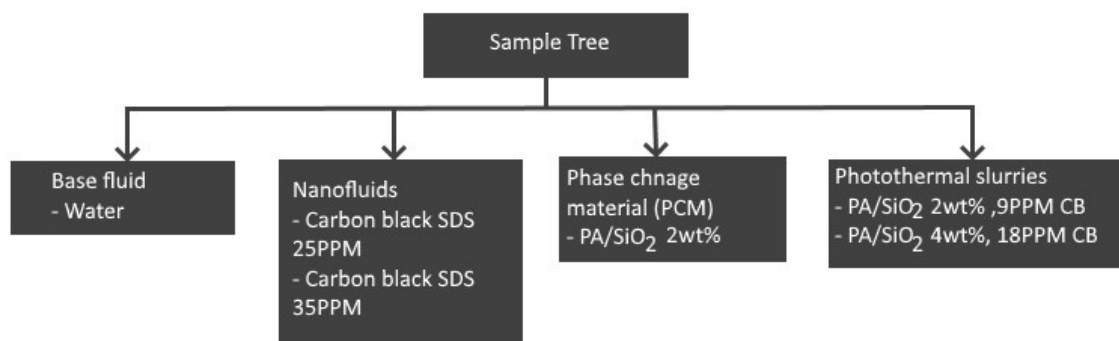


Figure 2.11: Samples used in the photothermal experiment.

### 2.4.1 Preparation and characterization

The carbon black nanofluids are produced by dispersing a known concentration of carbon black nanoparticle; with the particle size of less than  $30nm$ , in a known volume of distilled water, along with other stabilizing surfactants. Different concentration from 15PPM to 45PPM are prepared for photothermal testing.

The shape stabilized  $PA/SiO_2$  phase change material was prepared by sol-gel method and material characterization are performed by Scanning Electron microscopy (SEM). The SEM image of  $PA/SiO_2$  particles shows homogeneous and uniform spherical structure with diameters of  $200-300nm$ . The melting and solidifying curves of palmitic acid and  $PA/SiO_2$  is analyzed using Differential Scanning Calorimetry (DSC). From the DSC curves the  $PA/SiO_2$  starts melting at  $63.1^\circ C$  and freezing at  $59.2^\circ C$ , whereas the pure palmitic acid melts and solidifies at  $64.6^\circ C$  and  $60.4^\circ C$ , respectively. This data is referenced from [37] and the photograph of SEM and DSC are shown in Figure A3.1 and Figure A3.2 respectively in Appendix A3.

The photothermal slurry is prepared by dispersing a known concentration of carbon black and shape stabilized PCM particles by weight concentration, in water. It is then ultrasonicated at frequencies greater than  $20kHz$  so that the particles are not sedimented at the bottom. The stability of the slurry depends on the concentration, ultrasonication time and power. The prepared slurries are stable for at least 2 hours and sedimentation is dispersed by shaking or by ultrasonication[37]. The optical transmittance spectra of water are compared with 10wt%  $PA/SiO_2$ - 45PPM carbon black slurry, in the wavelength of  $200-2500nm$  at room temperatures, as shown in Figure A3.3. The slurry has the least transmittance of light in the

visible region compared to water, indicating high absorbance property, important for collecting sunlight irradiation.

The important physical and thermal properties that are used for further calculations are tabulated in Table 2.1.

**Table 2.1: Physical and thermal properties of the working fluid.**

Property	Value	Units
Density water ( $\rho_{water}$ )	1000	$kg/m^3$
Density carbon black ( $\rho_{CB}$ )	1700	$kg/m^3$
Density palmitic acid ( $\rho_{PA}$ )	853	$kg/m^3$
Density silica di-oxide ( $\rho_{SiO_2}$ )	2410	$kg/m^3$
Specific heat water ( $Cp_{water}$ )	4.182 - 4.205	$kJ/(kgK)$
Specific heat carbon black ( $Cp_{CB}$ )	710	$J/(kgK)$
Specific heat palmitic acid ( $Cp_{PA}$ )	1806	$J/(kgK)$
Specific heat silica di-oxide ( $Cp_{SiO_2}$ )	705	$J/(kgK)$
Peak melting temperature $PA/SiO_2$ ( $T_{m,peak}$ )	63.1	$^{\circ}C$
Latent heat $PA/SiO_2$ ( $\Delta H_m$ )	74.8	$kJ/kg$

## 2.5 Experimental procedure

The steps to power the instruments and setting up the sample for the photothermal experiment is outlined in this section.

### 2.5.1 Instrument phase

If the power output greater than 1.5 suns is required, then the high flux beam concentrator is added to the illuminator housing. For less than 1.5 suns, direct output from illuminator is used. The illuminator power switch and the power supply module is turned on. Next, the lamp power setting is configured in the power supply module. It is set to the desired mode, either constant power mode or constant current mode. In the constant power mode, the power limit is set in the range of +10% to -20% of the nominal lamp rating. After setting the desired power, the lamp start button on the power supply module turns on the solar simulator. It takes a few seconds to start the lamp. The illumination is controlled by using a shutter close/open switch. To ensure uniformity of irradiation in the working plane, a warm-up period of 30 minutes is given before placing the sample in the collector for the photothermal experiment. The power of the output beam is checked using the PV reference cell. If the desired output power is not attained, either lab jack height adjustments are made in the working distance ranging from 210 to 160 mm to have uniformity in the output beam, or the input power is adjusted on the power supply module.

The PV reference cell has an operating limit of up to 3 suns, hence it cannot be used with high flux beam concentrator. Therefore, when high beam concentrators are used, the intensity of irradiation at the working plane is theoretically determined as follows. From the test report of the solar simulator supplier, the silicon test cell had a reading of 8.5mA (equivalent to 1 sun) without beam concentrator at a working distance of 304.8mm. With beam concentrator, the

silicon test cell had an output of 80.7mA at 50.8mm working distance. During the experiment, the sample will be placed at 63.5mm from the beam concentrator because the output beam from the concentrator is uniform\flattest at this working distance as provided in the beam concentrator report. From the above data, the output current is linearly interpolated and determined to be 77.09mA at 63.5mm working distance. The ratio of silicon test cell output with beam concentrator, to the silicon cell output without beam concentrator, determines the magnification factor. Using the PV reference cell, the intensity without the beam concentrator at a working distance of 63.5mm is determined to be 0.865 sun. Intensity without beam concentrator multiplied with the magnification factor determines the intensity with beam concentrator and found to be 7.8 suns. The general instrument phase outline is shown in the schematic 2.12.

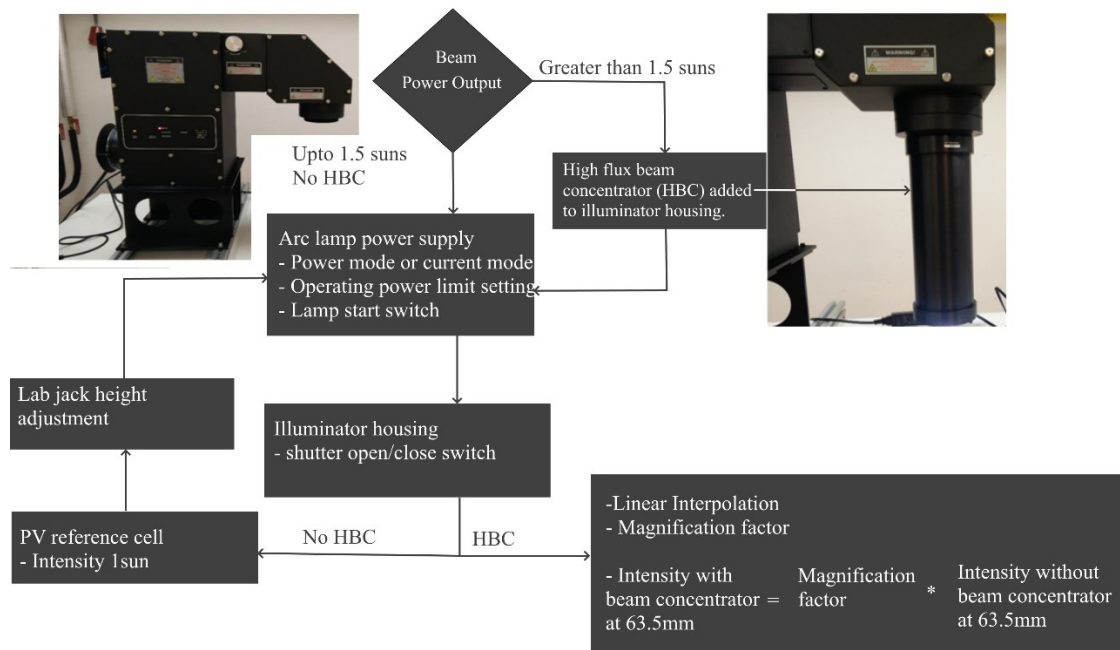


Figure 2.12: Instrument phase schematic.

The other instrument used for the experiment are thermocouples and DAQ system, these are controlled via LABVIEW software. The calibrated thermometer equations are implemented in the LabVIEW graphical programming language. On running the program, the DAQ starts collecting the temperature data. The collected data is stored on the computer in the excel file format. This data is later retrieved and used for analysis using Python programming language.

### 2.5.2 Sample phase

The sample is checked for sedimentation, to redistribute the sample is ultrasonicated before transferring to the collector. On a precision weight measuring scale, an empty vial container is weighed. Next, the volume of the inner cylinder of the collector is known (21.5ml), in which the sample is placed for irradiation. This same volume of sample (21.5ml) is transferred to a vial container with the help of a 10ml pipette. Again the vial container is measured with the sample. The difference between the vial with sample and empty vial helps to determine the amount of sample that is to be under irradiation.

The RTD's are already placed in the collector, as described in section 2.2.3. In addition to measuring temperature, RTD's stops any leakage through the holes drilled to place the RTD and furthermore it is sealed externally. Then, the known amount of sample is transferred to the collector with the help of a pipette. Further, the sample is filled till the upper edge (height=38.5mm) of the collector. Next, the quartz glass is placed on the filled collector, the excess sample flows out and is removed using a pipette. The excess sample added to the collector, to ensure no air bubbles are formed during the process of placing the quartz glass. The quartz glass acts as a sealant minimizing heat losses with the ambient. This whole assembly is placed under the solar illuminator for approximately 5400s to 9000s and the temperatures are recorded in the computer using the data acquisition system. The sample phase is pictorially represented as shown below. After the experiment, the used sample is removed and the collector is cleaned using isopropyl alcohol and the procedure is repeated for different samples.

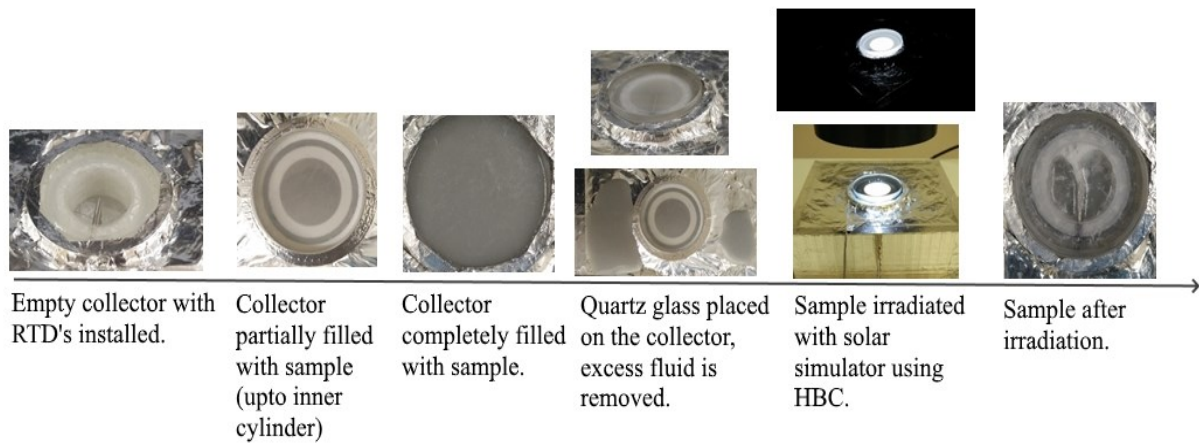


Figure 2:13: Sample phase schematic.

## Chapter 3

### Results and Discussion

In this chapter, the experimental data is analyzed and the important results are discussed. In the first section, the temperature profile under low and high intensity are studied. The effects of collector height and irradiation time on temperature are discussed. In the subsequent sections, the collector efficiency and thermal storage are studied taking collector height and radiation time as the variable parameters.

#### 3.1 Temperature distributions

The light from the artificial sun is absorbed by the working fluid in the DASC system and the light energy is converted into heat, thereby increasing the fluid temperature. At a given intensity of solar irradiation, the rate of temperature increase depends on the heat capacity, optical properties and thermal conductivity of the working fluid. The photothermal conversion performance of different working fluids is tested using a solar simulator with a solar flux of  $1000 \frac{W}{m^2}$  and  $7800 \frac{W}{m^2}$ .

During the instrument phase as discussed in section 2.5.1, the solar intensity is adjusted to  $1000 \frac{W}{m^2}$  (1 sun) by varying the height of illumination. The average temperature as a function of time and intensity level of 1 sun, for base fluid, is shown in figure 3.1, the water tends to reach a uniform temperature along the height of the collector. After irradiation time of 9000s, the maximum temperature reached by water at the top of the collector is  $41.19^\circ\text{C}$  and the overall maximum bulk temperature reached is  $39.94^\circ\text{C}$ . For the same irradiation time, the maximum temperature difference between the first thermometer and last thermometer is  $1.25^\circ\text{C}$ . The temperature gradient along with the height of the collector, at the end of the irradiation, is determined to be  $0.041^\circ\text{C}/\text{mm}$ . The slope of the temperature-time plot decreases with increase in time, which is due to the rise in the temperature difference between the working fluid and the surrounding ambient, resulting in higher heat losses.

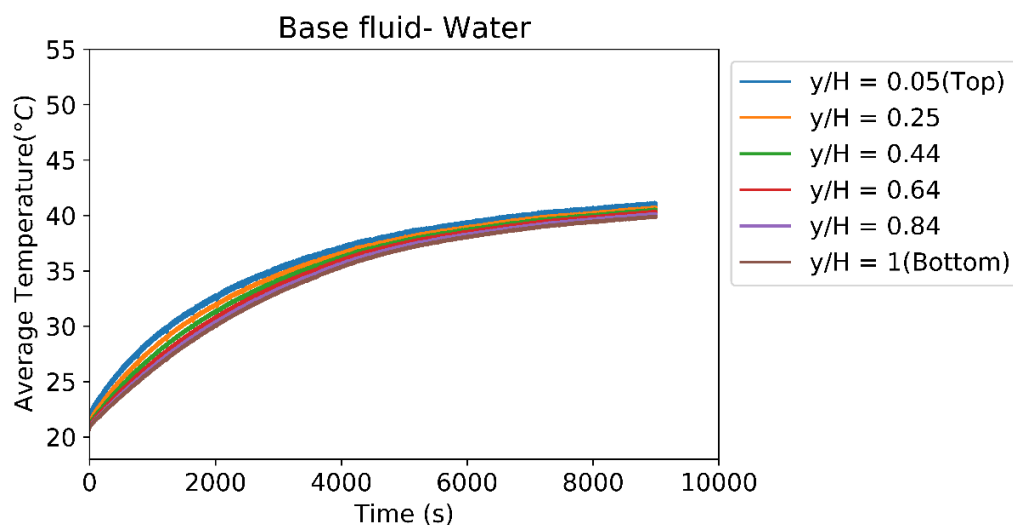


Figure 3.1: Average temperature measured for base fluid (water) at 1 sun irradiation.

Figure 3.2 shows the average temperature variation with time for nanofluid with 45PPM carbon black (CB) particle. In comparison to water, the nanofluid has higher temperature increment as seen in the plot. The rate of rising in temperature is steep for the nanofluid in the first 2000s due to the small temperature difference between the working fluid and the environment. After 2000s the slope gradually tends to reduce, because of the increased heat losses with the ambient, causing the working fluid temperature to reach an equilibrium temperature with the surrounding. The maximum temperature achieved by this nanofluid after 9000s at the top of the collector and overall bulk temperature along the height of the collector is 50.40°C and 44.43°C respectively. Compared to base fluid, nanofluid shows a 22.35% temperature increase at the top of the collector and 11.24% considering the complete collector. This enhancement in temperature rise is due to the carbon nanoparticles dispersed in the base fluid.

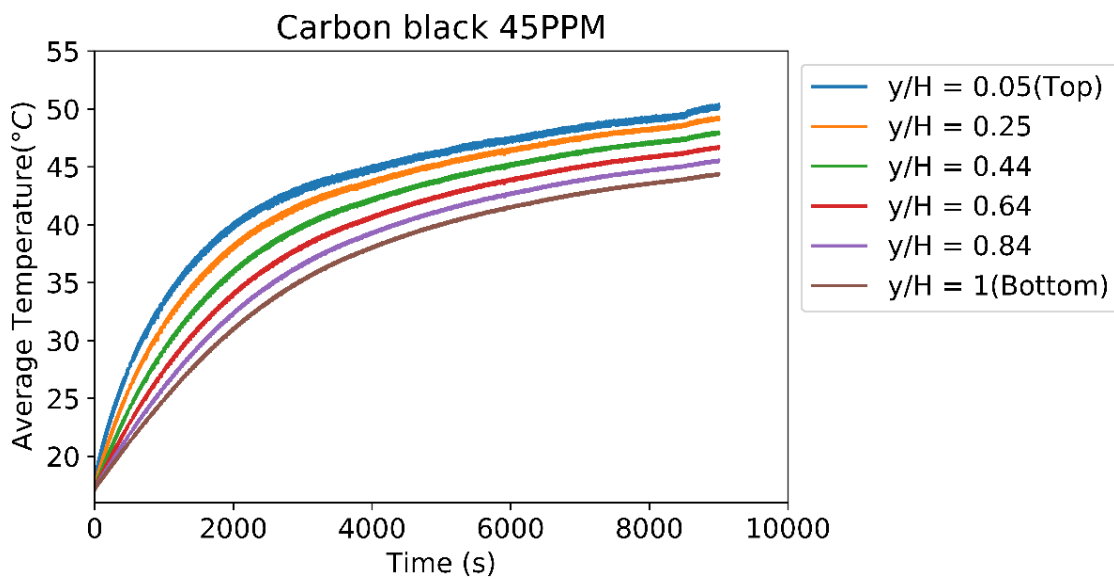


Figure 3.2: Average temperature as a function of time at 1 Sun irradiation for carbon black 45PPM.

Figure 3.3 displays the behavior of the slurry containing PCM and carbon black nanoparticles ( $PA/SiO_2$  10wt%- 45PPM CB slurry). The temperature profile is comparable with that of the nanofluid in figure 3.2, but the temperature-time slope is less steep compared to the nanofluid. When compared with the base fluid in figure 3.1, the slope of the nano slurry is steeper, with a gradual decrease in temperature along with the height of the collector. For the same amount of solar intensity of 1 suns and irradiation time of 9000s, the maximum temperature at the first RTD location ( $y/H=0.05$ ) and the bulk average temperature ( $y/H=1$ ) of the slurry are 46.02°C and 40.15°C, respectively. However, this resulted in a temperature reduction of 8.69% at  $y/H=0.05$  and 9.63% at  $y/H=1$  compared to CB nanofluid. On the contrary, to water, the maximum temperature incremented by 11.72% at the top of the collector. Whereas at the bottom of the collector ( $y/H=1$ ) the temperature is comparable with that of water, the reason is that as the slurry is more opaque, which decreases the transmittance of light with an increase in collector height. Table 3.1 summaries the average temperature after 9000s of irradiation, for all the above samples discussed.

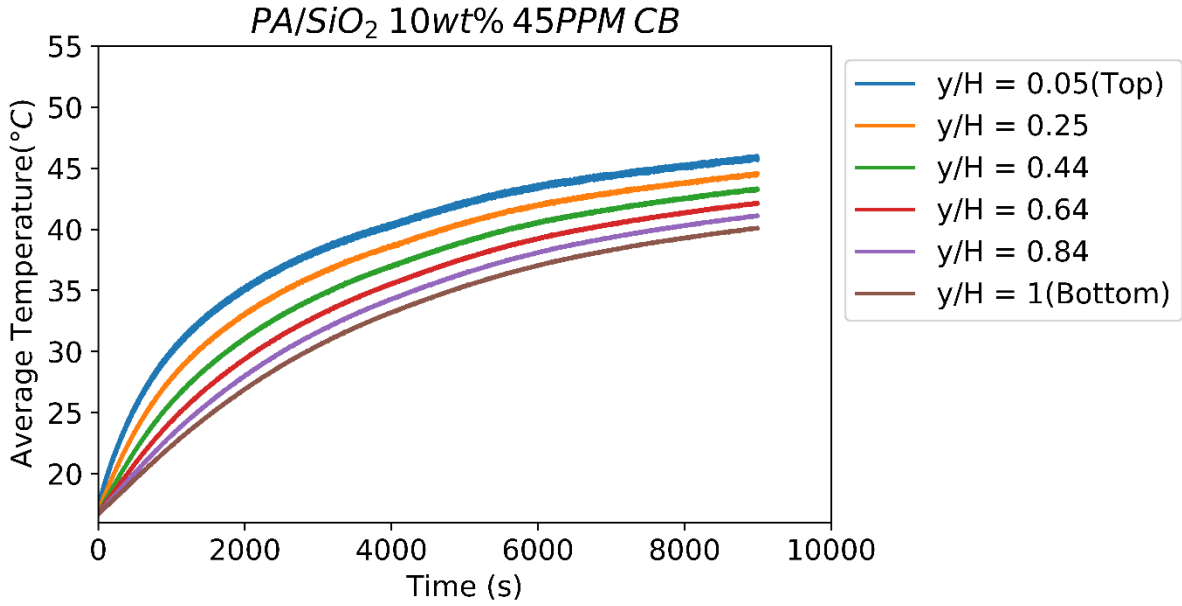


Figure 3.3: Average temperature as a function of time with 1 Sun irradiation for  $PA/SiO_2$  10wt%-45PPM.

**Table 3.1: Average temperature summary after 9000s.**

Samples	Height $y/H=0.05$		Height $y/H=1$	
	Average Temperature (°C)	Temperature increase compared to water (%)	Average Temperature (°C)	Temperature increase compared to water (%)
Water	41.19	-	39.94	-
45PPM CB - nanofluid	50.40	22.35	44.43	11.24
10wt% $PA/SiO_2$ -45PPM CB slurry	46.02	11.72	40.15	0.5

To analyze the thermal storage performance of  $PA/SiO_2$  10wt% - 45PPM CB slurry with a peak phase change temperature at  $63.1^\circ\text{C}$ , the sample is irradiated with 1sun intensity, for a duration of 23400s (6.5 hours) as shown in figure 3.4. From the plot, it is clear that the temperature tends to reach an equilibrium with the ambient. The maximum temperature achieved at the top of the collector ( $y/H=0.05$ ) after 6.5 hours of 1 sun irradiation is  $50.30^\circ\text{C}$ . This temperature is far below than the required peak phase change temperature. Therefore further experiments were performed by installing high flux beam concentrator (HBC) with an intensity of approximately  $7800 \frac{W}{m^2}$ , at the working plane of  $63.5\text{mm}$  from the HBC, as will be discussed next.

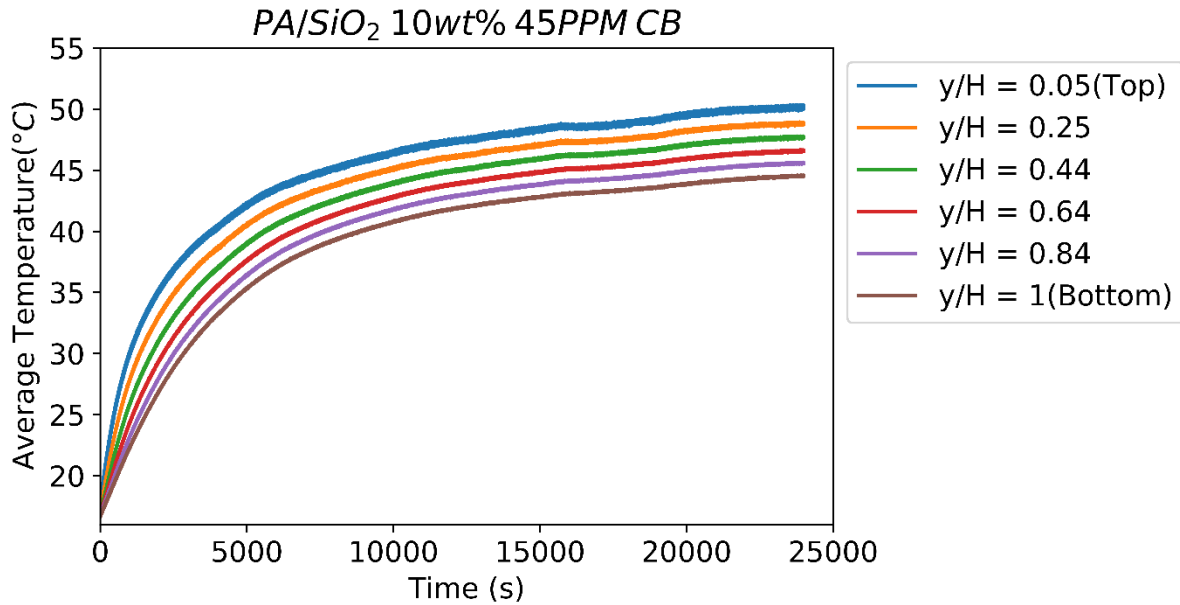


Figure 3.4: Average temperature as a function of time with 1 Sun irradiation of  $PA/SiO_2$  10wt% 45PPM till 25000s.

The temperature variation of different working fluids along the height for a time duration of 3000s, for a high-intensity solar radiation, is shown in figure 3.5. In the plots, 0mm collector height represents the top of the collector and 30mm the bottom of the collector. As observed in the contour plot 3.5, the maximum temperature change is seen at the top part of the collector at any given instant of time, except for water. Another observation from the contour plots at the end of 3000s, in the top part of the collector, is that the temperature gradients are decreasing in the following order: CB nanofluid,  $PA/SiO_2$ - CB slurry, plain  $PA/SiO_2$  2wt% and finally water.

The temperature gradient for water is almost close to zero at any given time, indicating uniform heating of the base fluid. For all other samples during the radiation time of 3000s, a non-uniform temperature is seen along the collector height. This non-uniform temperature along the depth is because of the added micro and nanoparticles to the base fluid. These added particles absorb the energy from the incident radiation and increase the fluid temperature. This rapid rise in temperature in the top section of the collector creates a temperature gradient in the remaining part of the collector. Even though the added nanoparticles help to achieve a high temperature in a short amount of time, but will not create a uniform temperature throughout the collector volume. The reason is that part of the incoming light is blocked or reflected by the added particles, and also the photon energy deteriorates in the depth direction[38]. Consequently, for the bottom part of the DASC, the prominent part of the heat source/temperature driving force is the conduction from the upper high-temperature fluid.

From the contour plots, for all the samples, it can be generally observed that the temperature rises with an increase in time. But the maximum temperature reached varies, depending on the concentration of the dispersed particles, collector height, and irradiation time. The following section is focused to further understand the temperature variation with time.

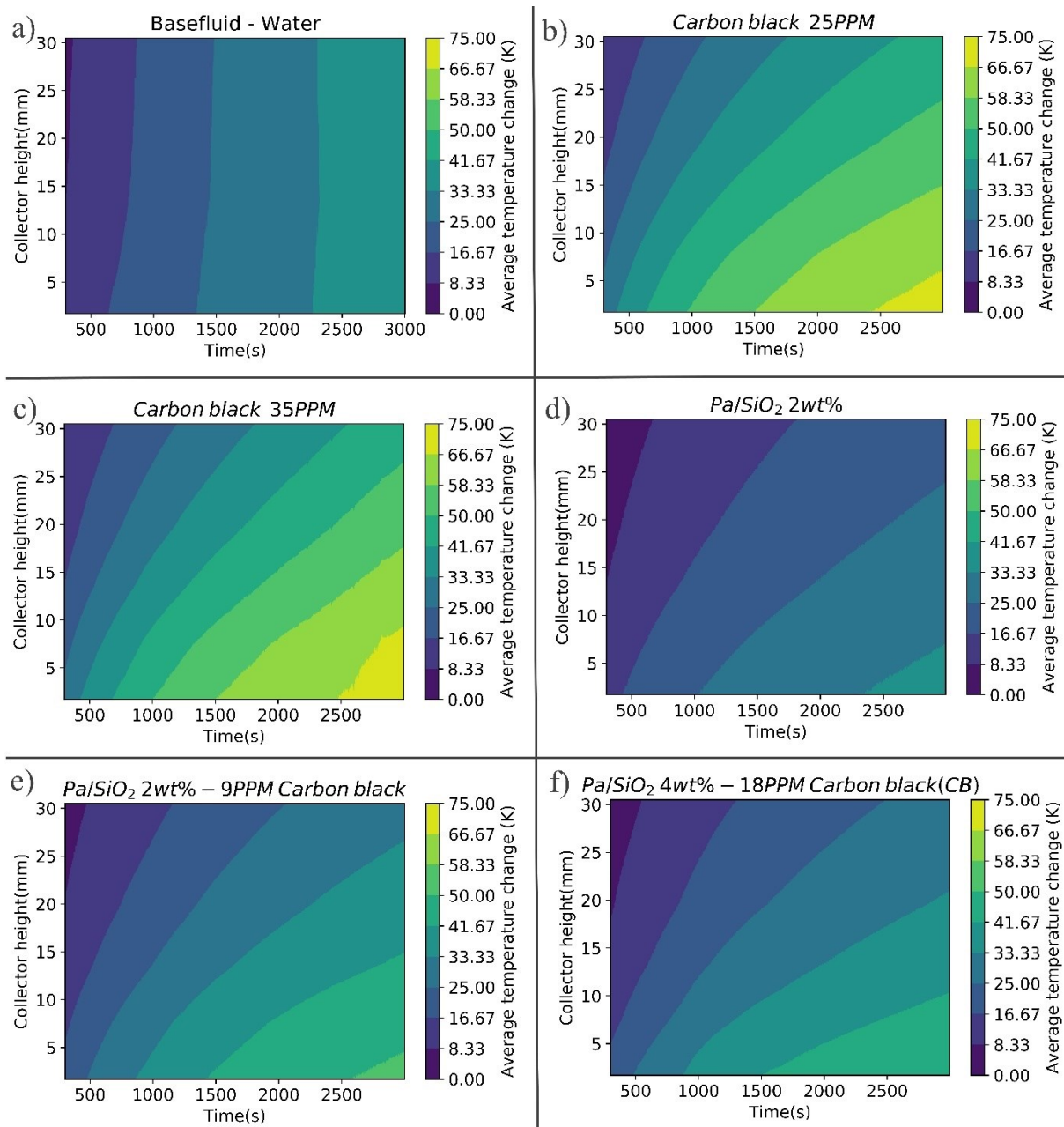


Figure 3.5: Temperature profiles at different heights and time up to 3000s; for a) base fluid - water, b) CB 25PPM, c) CB 35PPM, d)  $Pa/SiO_2$  2wt%, e)  $PA/SiO_2$  2wt%-9PPM CB, f)  $PA/SiO_2$  -4wt% 18PPM CB.

- **Effect of irradiation time:**

The irradiation time is the duration for which the fluids are exposed to the irradiation. The longer the exposure, higher the temperature. But, after certain time the rise in temperature is not significant and it affects the overall collector efficiency. Therefore, it is important to understand the heating rate behavior of nanofluid and PCM slurries with respect to water. To study the effects of exposure time on photothermal performances of the samples, and to achieve a phase change temperature throughout the collector height, the water and PCM slurry samples were irradiated continuously up to 9000s. While the CB nanofluids are only 3000s exposed to solar illumination, because it reaches high temperature quickly and further heating would lead to boiling of water, resulting in undesirable effects on the particle concentration.

Figure 3.6 and 3.7, presents the temperature profile at top ( $y/H=0.05$ ) and bottom ( $y/H=1$ ) of the collector height, respectively: for base fluid; nanofluids with CB concentration of 25PPM and 35PPM;  $PA/SiO_2$  2wt%;  $PA/SiO_2$  2wt%- 9PPM CB slurry; and  $PA/SiO_2$  4wt%-18PPM CB slurry as shown in the figure legend.

In the initial 1800s, at the top of the collector ( $\frac{y}{H} = 0.05$ , figure 3.6), the curves of carbon black samples and  $PA/SiO_2$  – carbon black slurry samples show a sharp rise in temperature compared to water. The nanoparticles effective photon capture and molecular heating property attribute to the sharp increase in temperature behavior of the CB nanofluids and PCM slurries. Besides, the temperature rise of  $PA/SiO_2$  2wt%- 9PPM CB slurry is 31.58% better than the pure  $PA/SiO_2$  2wt%, again indicating the ability of carbon black as a good photon absorber.

After 1800s at the same height, rate of temperature growth for all the sample reduces, mainly because the temperature difference between the collector and the ambient increases, causing more convective heat losses from the top of the collector [39]. The carbon black sample attains a temperature of 90°C within 3000s, while other samples are still below 65°C. In the case of  $PA/SiO_2$  – CB slurries reach a phase change onset temperature, hence the decline in slope indicating the latent heat storage, this will be further addressed in the thermal storage section.

At the end of 9000s of irradiation for the same height,  $PA/SiO_2$  4wt%-18PPM CB slurry reaches the highest temperature of 85.5°C, followed by  $PA/SiO_2$  2wt%-9PPM CB slurry (81.09°C), next by water (73.4°C), and finally  $PA/SiO_2$  2wt%. This  $PA/SiO_2$ -CB slurry reaching the maximum temperature at the end of irradiation is due to the extra carbon black nanoparticles in the slurry.

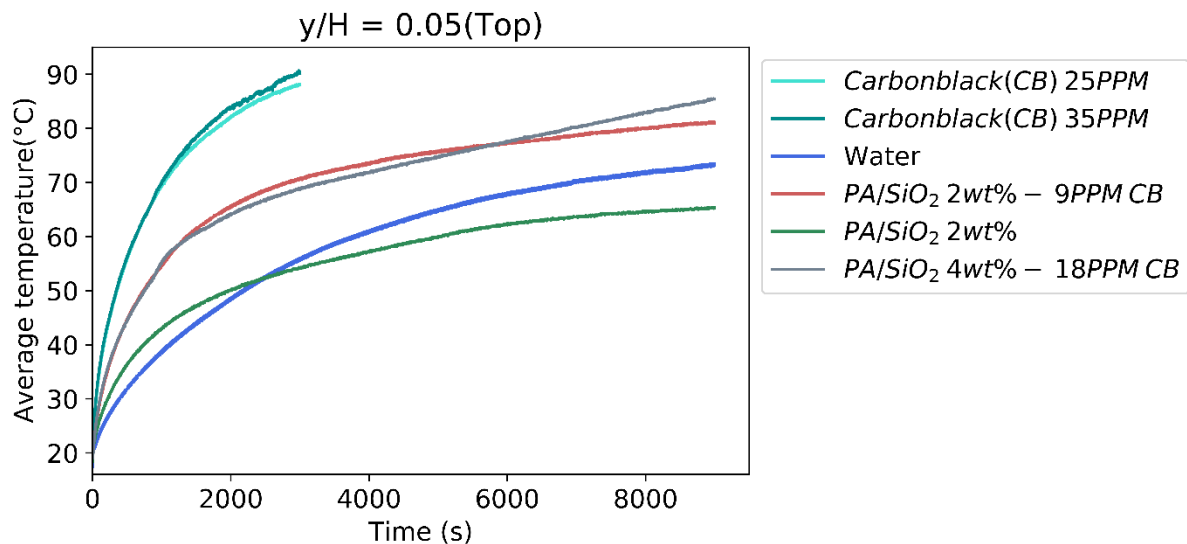


Figure 3.6: Temperature as a function of time, for different samples at  $y/H=0.05$ .

At the bottom of the collector ( $y/H=1$ , figure 3.7), temperatures of all the samples are lower than the temperatures at the top of the collector ( $y/H=0.05$ ), except for water. For instance, at 1800s, the temperature of  $PA/SiO_2$  2wt%-9PPM CB slurry is 0.63 times lower than the temperature at the top of the collector. The drop in temperature is because of the attenuation of radiation along with the height of the collector[38].

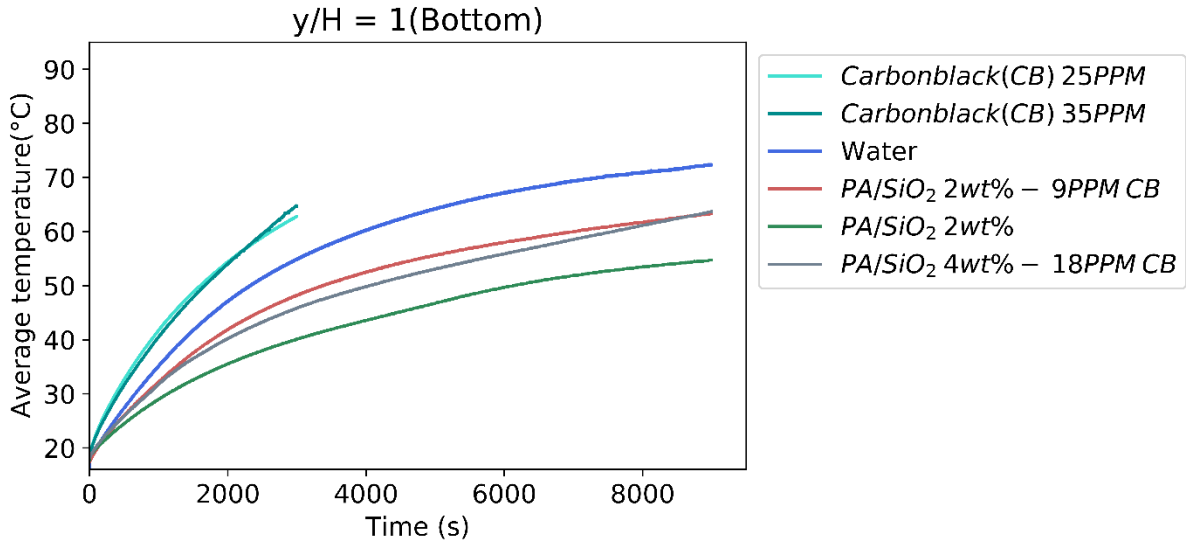


Figure 3.7: Average temperature as a function of time, for different samples at  $y/H=1$ .

Table 3.2 shows the summary of the average temperature increment and decrement of the samples, compared to water at heights  $y/H=0.05$  and  $y/H=1$ , for a different time. Thus from the table at  $y/H=0.05$ , the rate of rising in temperature is highest for the CB nanofluids, because of the higher concentration of nanoparticles compared to the CB nanoparticles in the  $PA/SiO_2 - CB$  slurries. In the case of  $PA/SiO_2 - CB$  slurries the minimum enhancement is achieved at the end of irradiation at the top of the collector. In contrast, at the bottom of the collector ( $y/H=1$ ) throughout the irradiation time, PCM slurries temperature is not enhanced, due to the reduced transparency of the photo-thermal slurries. However, the negative sign for the CB nanofluids ( $y/H=1$ ) indicates the increment in the temperature compared to water. Therefore up to 3000s, CB nanofluids achieves high temperature, irrespective of collector height.

**Table 3.2: Summary of temperature variation compared to water at top and bottom of the collector for different time.**

Time(s) Samples	Temperature increment (%) with reference to water at height $y/H=0.05$			Temperature decrease (%) with reference to water at height $y/H=1$		
	1800	3000	9000	1800	3000	9000
25PPM CB - nanofluid	71.4	57.7	-	-15.7	-14.6	-
35PPM CB - nanofluid	75.6	61.6	-	-14.6	-17.9	-
$PA/SiO_2$ 2wt%- 9PPM CB slurry	37.4	26.7	10.5	10.4	12	12.7
$PA/SiO_2$ 4wt%- 18PPM CB slurry	34.3	23.5	16.5	13.9	16.3	12

- **Effect of height:**

In the design of the collector for DASC, collector height is an important parameter because it determines the amount of sample to be used in the application. From the above analysis, the temperature of the slurries at the bottom of the collector is less than water (i.e., the bulk temperature of slurries are less than the water and hence low photo-thermal performance of the slurries). To determine the optimum collector height at which the performance of slurries is better than water at any instant of time, figure 3.8 is analyzed.

The pure  $PA/SiO_2$  2wt% sample has a higher temperature up to a depth of  $y/H=0.25$  (7.6 mm) in the initial 600s, compared to the water. Later, as the irradiation continues, the rate of temperature gradient of  $PA/SiO_2$  2wt% drops significantly as compared to water and  $PA/SiO_2$  2wt%- 9PPM CB slurry, indicated in the plot 3.8b to 3.8e. The possible reason for the decline in the rate of the temperature gradient is because of the physical nature of the sample, which is white, and this makes the absorption of solar radiation difficult in higher depths. As a result, to perform better than water, the  $PA/SiO_2$  2wt% should be limited to a collector height of  $y/H=0.25$  and irradiation of 600s.

From figure 3.8, the change in temperature of  $PA/SiO_2$ -CB slurries do not completely outperform the water, but depending on collector height and the time of irradiation the nano slurries performs better than base fluid. Table 3.3 summarizes the optimum collector height for which slurry performance is better at a given irradiation time. Based on the trend in the table 3.3, it can be generalized as follows: with an increase in time the required height of the collector for slurries reduces. Also, the rate of declination in collector height reduces after 3000s, this could be due to the decrease in the rate of temperature rise of the slurries. This behavior is associated with the phase transition. Moreover, as the collector height decreases, the temperature enhancement improves (i.e. at a given time, the temperature enhancement is minimum when the collector height is maximum). Beyond the mentioned threshold height at the corresponding time, the temperature change of water is more, the reason being the slurries are opaque compared to water, reducing the photon energy.

**Table 3.3: Optimum collector height for  $PA/SiO_2$ -CB slurries based on temperature increment compared to water**

Samples	Irradiation time(s)	Height- $y/H$ (mm)	Temperature increment compared to water (%)
$PA/SiO_2$ 2wt%- 9PPM CB slurry	600	0.64 (19.5)	13.1
	3000	0.44 (13.5)	10.9
	3600	0.44 (13.5)	8.7
	7200	0.25 (7.6)	8.4
	9000	0.25 (7.6)	7.5
$PA/SiO_2$ 4wt%- 18PPM CB slurry	600	0.64 (19.5)	5
	3000	0.44 (13.5)	4.2
	3600	0.25(7.6)	11
	7200	0.25 (7.6)	6.8
	9000	0.25 (7.6)	11.1

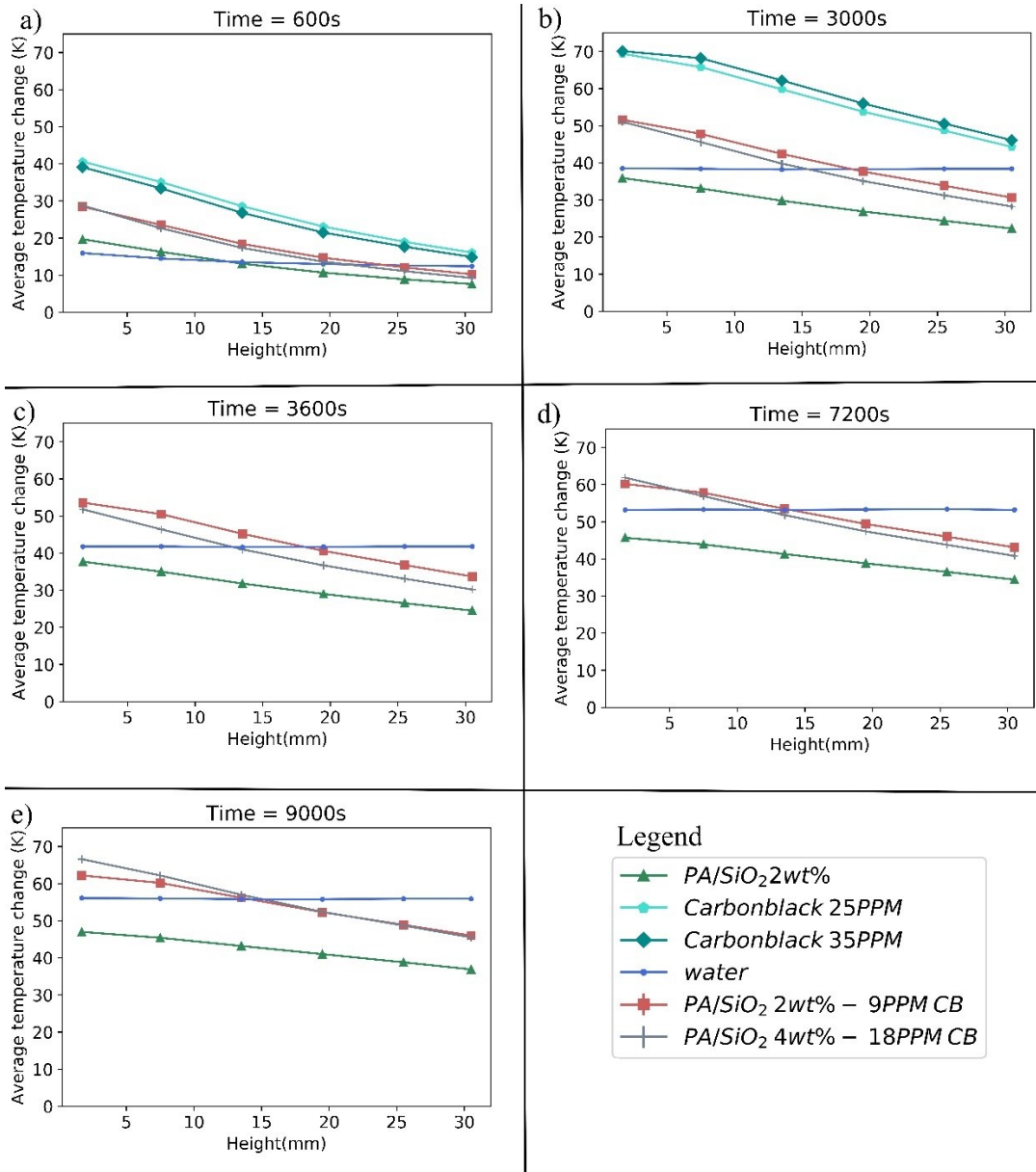


Figure 3.8: Temperature variation with depth at the irradiation time of a)600s, b)3000s, c) 3600s, d)7200s, e) 9000s.

### 3.2 Efficiency

The photothermal performance of the used working fluid determines the collector efficiency. The base fluid and slurries performance are calculated using Eq 2.7 and Eq 2.13, respectively. The assumptions used for the calculations are as follows:

- a) The collector walls are completely adiabatic, and
- b) heat losses by convection and radiation with the surrounding environment occurs only from the top of the collector[18].

To determine overall collector efficiency, the bulk temperature of the fluid calculated from the arithmetic mean of temperature measurements at different heights are used. The photo-thermal conversion efficiency as a function of collector height and irradiation time up to 3000s, for base fluid, carbon nanofluid and slurries are represented in the contour plot 3.9. The general observation from figure 3.9a) to 3.9f) are:

- The efficiency increases with height, but decreases with time, irrespective of the samples considered.
- Although the temperature rise in the top of the collector is maximum. But at the corresponding height, the efficiency is minimum because of the decline in the rate of temperature change.
- The efficiency is maximum at the bottom of the collector mainly because of the large amount of the working fluid, at a particular instant of time.
- Carbon black fluids with 25PPM and 35PPM concentrations, perform better compared to water, due to the higher thermal conductivity of the added carbon particles.
- $PA/SiO_2$  - CB slurries are more efficient than just  $PA/SiO_2$ , this is again due to the presence of highly conductive carbon particles.
- The overall performance of the base fluid is better than the plain  $PA/SiO_2$  sample.
- The performance comparison between base fluid and  $PA/SiO_2$  - CB slurries depends on the operating parameters like receiver height, irradiation time and particle concentration.
- The water efficiency at the bottom of the collector is maximum when compared to photo-thermal slurries the reason is again the reduced transparency of the slurries at large depths.

Furthermore, the efficiency of the PCM slurries is compared to that of water for total irradiation of 9000s as continued below.

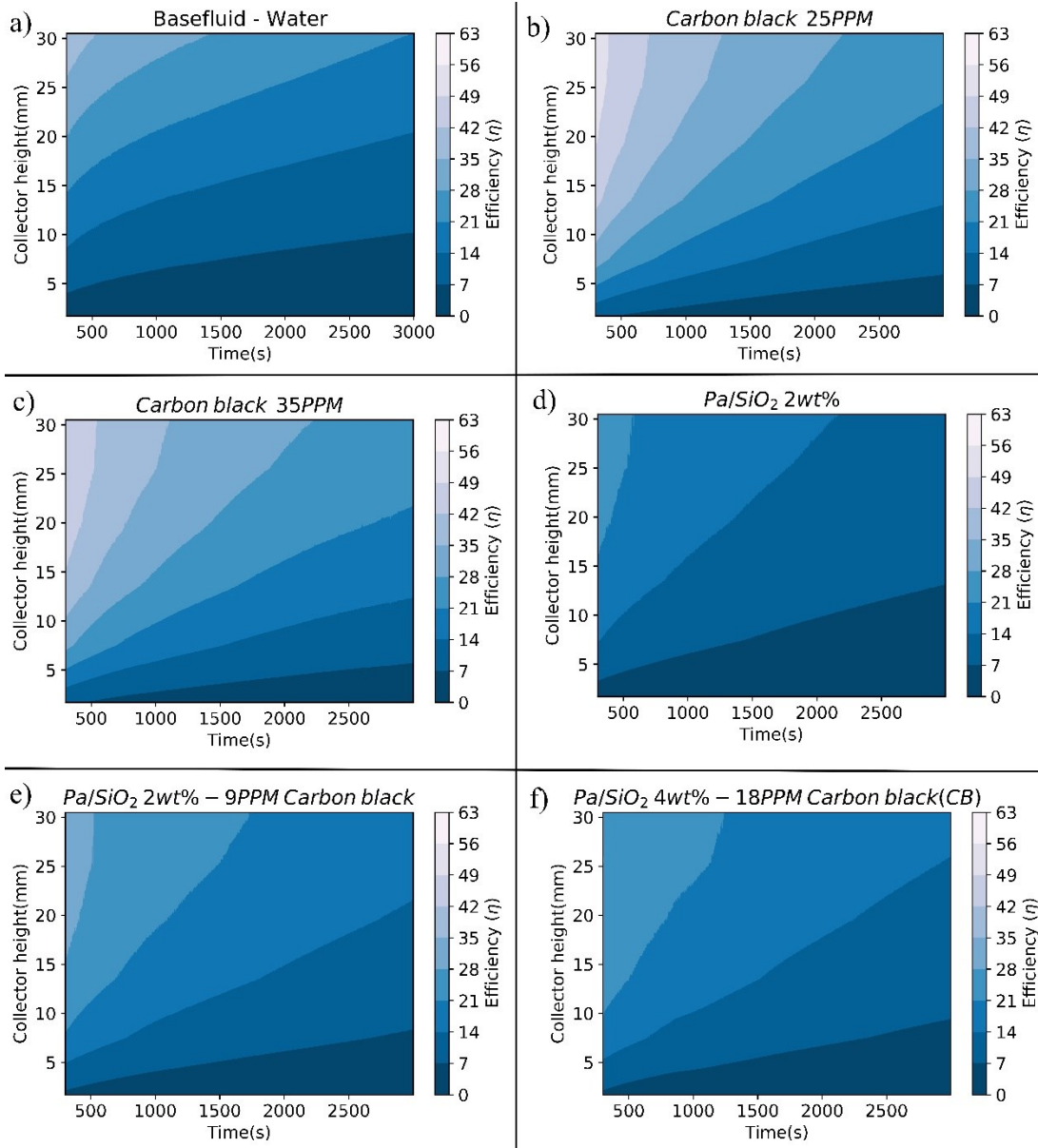


Figure 3.9: Collector efficiencies as a function of collector height and irradiation time for a) base fluid, b) CB 25PPM, c) CB 35PPM, d)  $Pa/SiO_2$  2wt%, e)  $Pa/SiO_2$  2wt%- 9PPM CB, f)  $Pa/SiO_2$  4wt%-18PPM CB.

At receiver height of  $\frac{y}{H} = 0.05$  (figure 3.10a) the maximum efficiency achieved by the CB nanofluids at 300s is within 10% and the efficiency reduces with time. The efficiency is small because of the mass corresponding to this height is low. A similar trend of decline in efficiency with time is observed in the bottom part of the collector (figure 3.10b), expect the efficiency has reached a higher value with depth. This increment in efficiency is mainly because of the increased volume, and the fluid in the lower part of the collector has minimum losses with the ambient compared to the top surface. In contrast to the top of the collector, the efficiency of PCM slurries is lower than the water. After 5400s, the rate of efficiency decline is not significant, because the collector system is trying to attain a steady-state. Therefore, with an increase in irradiation time, the efficiency drop evens out. Table 3.4 presents the efficiency variation as compared to water at different irradiation time. At the top of the collector the efficiency increment of the PCM slurries reduces with increase in time. The maximum

efficiency increment is observed for shorter duration of irradiation time. Whereas at the bottom of the collector the performance of water is better at any given instant of time.

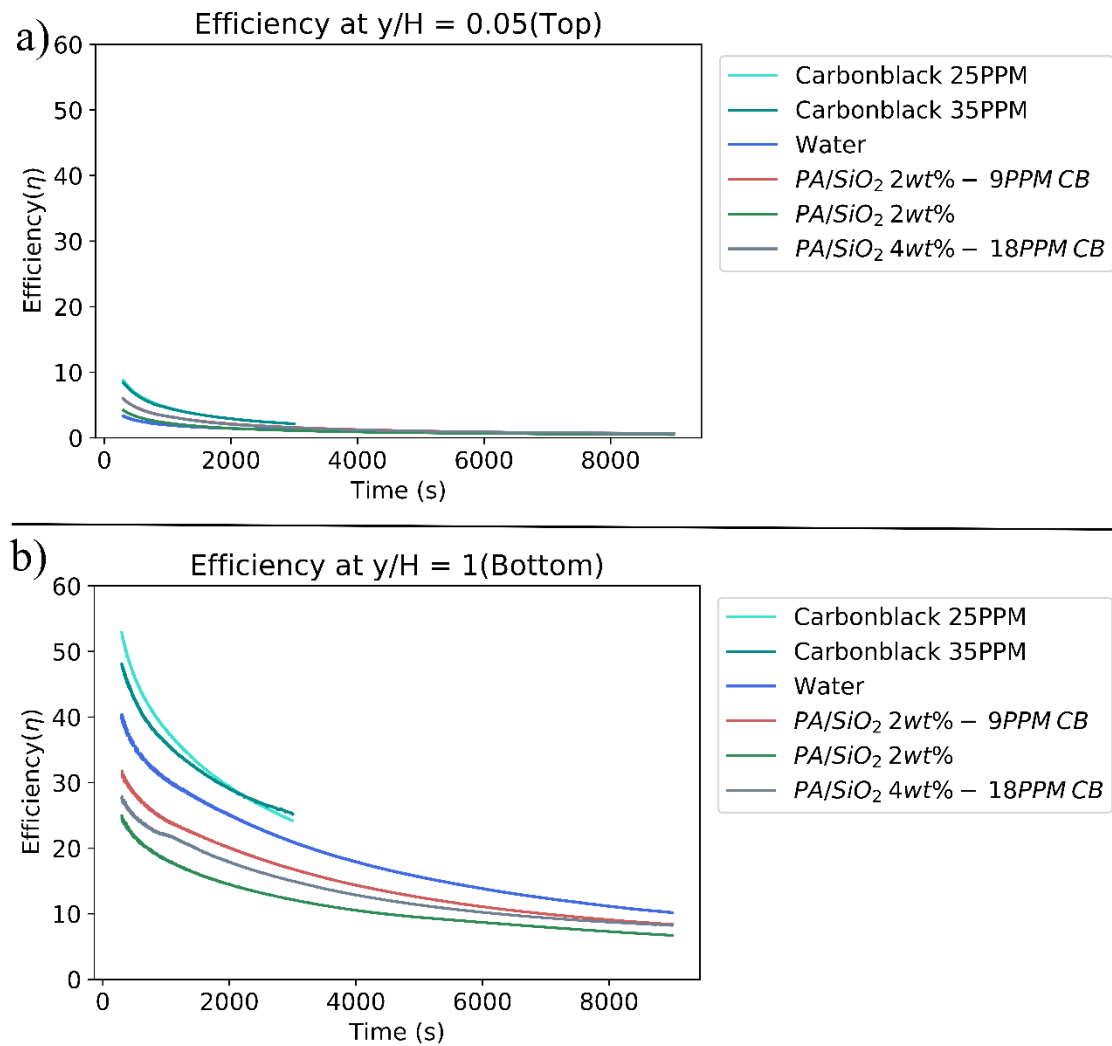


Figure 3.10: Collector efficiency as a function of irradiation time for different samples at height a)  $y/H = 0.05$  and b)  $y/H = 1$ .

**Table 3.4: Efficiency compared to water at top and bottom of the collector for different time.**

Time(s)	Efficiency increment (%) with reference to water at Height $y/H=0.05$			Efficiency decrease (%) with reference to water at Height $y/H=1$		
	1800	3000	9000	1800	3000	9000
Samples						
PA/SiO <sub>2</sub> 2wt%-9PPM CB slurry	52.6	34.2	10.5	20.1	19.8	17.8
PA/SiO <sub>2</sub> 4wt%-18PPM CB slurry	47.9	28.9	17.8	28.5	28.4	19.2

To sum up, as the temperature of the working fluid rises with time, the heat loss with the ambient also increases, causing a decline in the heating rate and thereby decreasing the overall

efficiency. Although the CB nanofluid and  $PA/SiO_2$ -CB slurries have been observed to have stronger absorption of solar energy, it is also associated with larger heat loss as the temperature difference between the sample and the ambient widens up. The rate of efficiency drop for CB nanofluid and  $PA/SiO_2$ -CB slurries, at a given height, is quicker than the water because the water reaches a uniform temperature and the possibility to attain equilibrium state is slower. Also, the working fluids with a high temperature in the top and a relatively low bulk temperature results in lower photo-thermal performance[18].

From the above study, we know the extreme cases of efficiencies (top and bottom). To determine the optimum receiver efficiency for effective solar energy utilization, the effect of collector height for 1 hour is considered. The longer irradiation duration is not considered because the efficiency enhancement is lower.

The variation of collector height on the collector efficiency up to 1 hour of irradiation time is as shown in the bar plots 3.11. By increasing the collector height, more sample volume can absorb the incident radiation, leading to higher efficiency. There is a certain threshold collector height, after which the collector efficiency would not be greatly enhanced.

The collector efficiency of carbon black samples and water are compared in a different time as indicated in figure 3.11a and 3.11b. The efficiencies of 25PPM and 35PPM nanofluids are comparable. The enhancement is maximum at the top of the collector and decreases in depth. The improvement is notably because of the presence of carbon particles. In the case of the  $Pa/SiO_2$ -CB slurries, the trade-off height for  $Pa/SiO_2$ -CB slurries decreases with an increase in radiation time.

Table 3.5 presents the efficiency of the working fluid to that of water up to 1hour. For the CB nanofluids, a minimum efficiency increment is possible with the complete collector size and maximum increment depends on the smallest possible collector size and irradiation time. For example, up to 3000s of irradiation a collector size of 30.5mm results in 1.2 times more efficient than water and maximum enhancement of 1.8 times than water is possible with collector size of 1.5mm.

In the case of  $Pa/SiO_2$ -CB slurries, a maximum collector height of  $y/H=0.64$  (19.5mm) can be used in the first 600s, to get a performance magnification of 1.1 times the water, and maximum enhancement of 1.8 is possible at  $y/H=0.05$  (1.5mm). At the end of 1 hour, the collector height reduces to  $y/H = 0.44$  (13.5mm) for  $Pa/SiO_2$ 2wt%-9PPMCB slurry. While, the 4wt%-18PPM slurry requires  $y/H = 0.25$  (7.6mm). Therefore, with an increase in illumination time, collector height required to have better performance reduces and the enhancement is also small in these conditions. This decrease in the collector height with time is due to the decreased rate of heating of the slurries along the height of the collector.

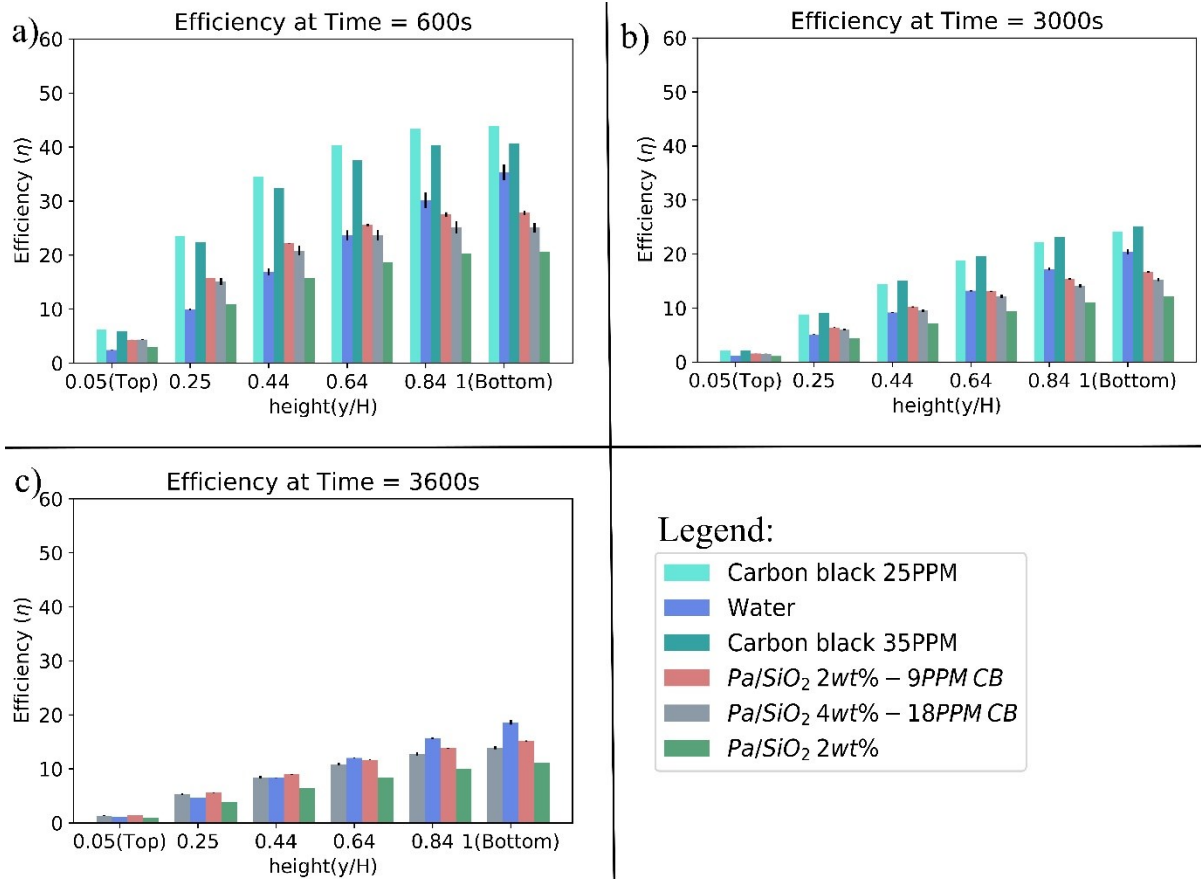


Figure 3.11: Collector efficiency as a function of height for water, Pa/SiO<sub>2</sub> and Pa/SiO<sub>2</sub>-CB slurries with irradiation time a) 600s, b) 3000s, and c) 3600s.

**Table 3.5: Efficiency comparison for all the fluids up to 1 hour at different height.**

Samples	Irradiation time(s)	Efficiency ratio compared to water at different height- y/H (mm)					
		0.05 (1.5 mm)	0.25 (7.6 mm)	0.44 (13.5 mm)	0.64 (19.5 mm)	0.84 (25.6 mm)	1 (30.5 mm)
25PPM CB nanofluids	600	2.6	2.4	2	1.7	1.4	1.2
	3000	1.8	1.7	1.6	1.4	1.3	1.2
35PPM CB nanofluids	600	2.5	2.3	1.9	1.6	1.3	1.2
	3000	1.8	1.8	1.6	1.5	1.3	1.2
PA/SiO <sub>2</sub> 2wt%- 9PPM CB slurry	600	1.8	1.6	1.3	1.1	0.9	0.8
	3000	1.3	1.3	1.1	0.9	0.8	0.8
	3600	1.3	1.2	1.1	0.9	0.8	0.8
PA/SiO <sub>2</sub> 4wt%- 18PPM CB slurry	600	1.8	1.5	1.2	1.1	0.8	0.7
	3000	1.3	1.2	1	0.9	0.8	0.8
	3600	1.3	1.1	1	0.9	0.8	0.7

### 3.3 Thermal storage

The latent heat released during the phase transition (uniform temperature), additionally adds to the sensible heat of the material. To understand the latent heat performance during the photo-thermal conversion, the thermal storage capacity of the DASCs based on water and the phase change material was calculated by equation 2.4 and 2.13. Figure 3.12 shows the energy density by the PCM samples and water, during the irradiation time, in three different collector heights (top, middle, and bottom).

In the upper part of the solar receiver ( $\frac{y}{H} = 0.05$ , figure 3.12a), all the samples exhibit an improvement in thermal heat density with increase of radiation time. The slurry containing 2wt% of  $Pa/SiO_2$  and 9PPM CB exhibits highest thermal storage capacity up to 5400s of irradiation, corresponding to the highest stagnation temperatures achieved by the slurry. After 5400s, the 4wt% of  $Pa/SiO_2$  and 18PPM CB achieves highest thermal storage density. The thermal heat density of the 2wt%-9PPM slurry is 1.2 times the base fluid at 5400s, while the 4wt%-18PPM slurry is also 1.2 times the base fluid but at 9000s. Therefore, the increased storage capacity is due to the existence of palmitic acid as PCM and CB in the slurries. Furthermore, with the rise in depth of the collector, the energy density decreases, because of the increase in the fluid volume.

In the middle part of the collector ( $\frac{y}{H} = 0.44$ , figure 3.12b),  $Pa/SiO_2$  2wt% -9PPM CB slurry stores 21.8% more energy than water at 1800s. As time reaches 3600s, the heat storage enhancement decreases to 8.26%, and this further reduces to 0.35% at the end of 9000s. The decrease in the change in temperature of the slurry affects the thermal energy stored. The decrease in change in temperature is due to the opaque nature of the thermal slurry. A similar trend is observed for the 4wt%-18PPM slurry. On the other hand, at the bottom of the collector ( $\frac{y}{H} = 1$ , figure 3.12c), the heat energy stored by the water is completely dominant at any given time. This is because the bulk temperature of the slurry is lower than that of water.

During the charging process, the embedded carbon black nanoparticles quickly absorb the incident solar radiation and convert to thermal energy, thereby increasing the temperature of the PCM and therefore the slurry temperature quickly increases. Further, the palmitic acid with phase change enthalpy of  $74.8J/g$ , could absorb a lot of heat in the melting process; acting as a heat sink in the slurries [9].

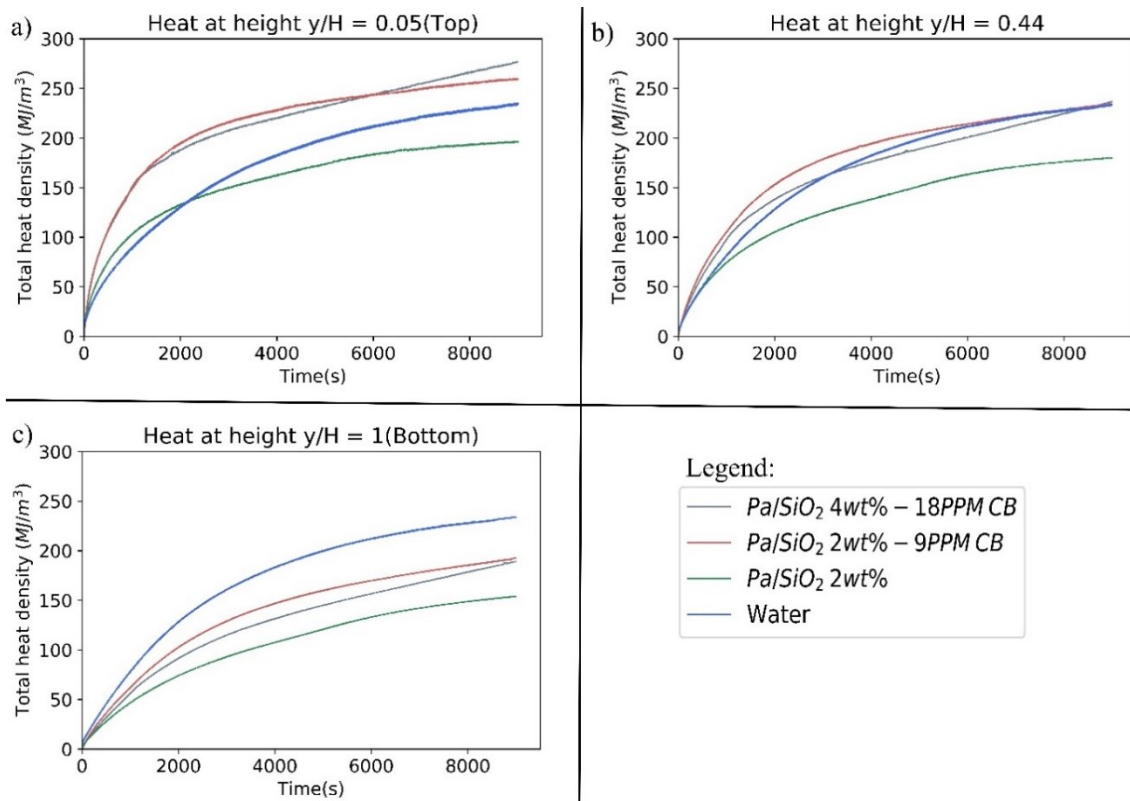


Figure 3.12: Thermal storage capacity of base fluid and the slurries containing different PCM for heights a)  $y/H=0.05$ , b)  $y/H = 0.44$ , c)  $y/H = 1$ .

In order to determine the phase change efficiency, the phase change peak temperature was determined from DSC results to be  $63.1^{\circ}\text{C}$  [37]. The phase transition of the PCM occurs at different time, height and particle concentrations. The time at which phase change occurs is determined, and at the same corresponding time, base fluid efficiencies are compared, as shown in figure 3.13. In figure 3.13, the variation of collector height is indicated on the bottom x-axis and the time at which peak phase change temperature reached is shown on the top x-axis.

The efficiency during the phase change of  $PA/SiO_2$  sample is compared with the efficiency of water at the corresponding phase change time as shown in figure 3.13a. Irrespective of height the  $PA/SiO_2$  sample has always lower efficiency than water, because of the low heating rate. Also,  $PA/SiO_2$  takes about 6476s (1.8 hours) to reach the peak phase change temperature at the top of the collector, because of lower absorption of heat. Even with thermal storage in the pure PCM fluid, the performance of the water is better.

The thermal storage efficiency of  $PA/SiO_2$  2wt%- 9PPM CB slurry is shown in figure 3.13b. As it can be observed, the efficiency during phase change of 2wt%-9PPM slurries is more efficient than water up to a collector height of  $y/H=0.44$  (13.5mm). After which the water is more efficient, in spite of the latent heat. This is because the sensible heat after  $y/H=0.44$  (corresponding to phase change time of 3726s) is still lower than water (i.e., the temperature rise of 2wt%-9PPM is lower than water). The initial phase transition occurs after 1863s at the top of the collector, and the phase change efficiency is 48.6% higher than water. The next peak phase change occurs after 600s at  $y/H = 0.25$  with an increment in the efficiency of 31.56%. At collector height  $y/H=0.44$  and for the illumination of 3600s the 2wt%-9PPM slurry stores 8.26% more energy than water. The complete collector (volume=21.5ml) takes almost 2.5hours

to reach peak phase change temperature (completely charged), but the efficiency of water is higher than the  $PA/SiO_2$  2wt%- 9PPM CB slurry with phase change.

In the case of  $PA/SiO_2$  4wt%- 18PPM carbon black slurry (figure 3.13c), the phase change efficiency is only efficient up to a collector height  $y/H = 0.25$  (7.5mm). At this height, it takes about 3000s to reach a peak phase change temperature with an energy storage improvement of 16.17%. In the top part of the collector  $y/H=0.05$ , the heat storage of 4wt%-18PPM slurry is enhanced by 50.34% at 1820s. Therefore, heat storage improvement is appreciable in shorter segment of the collector and for short duration of time.

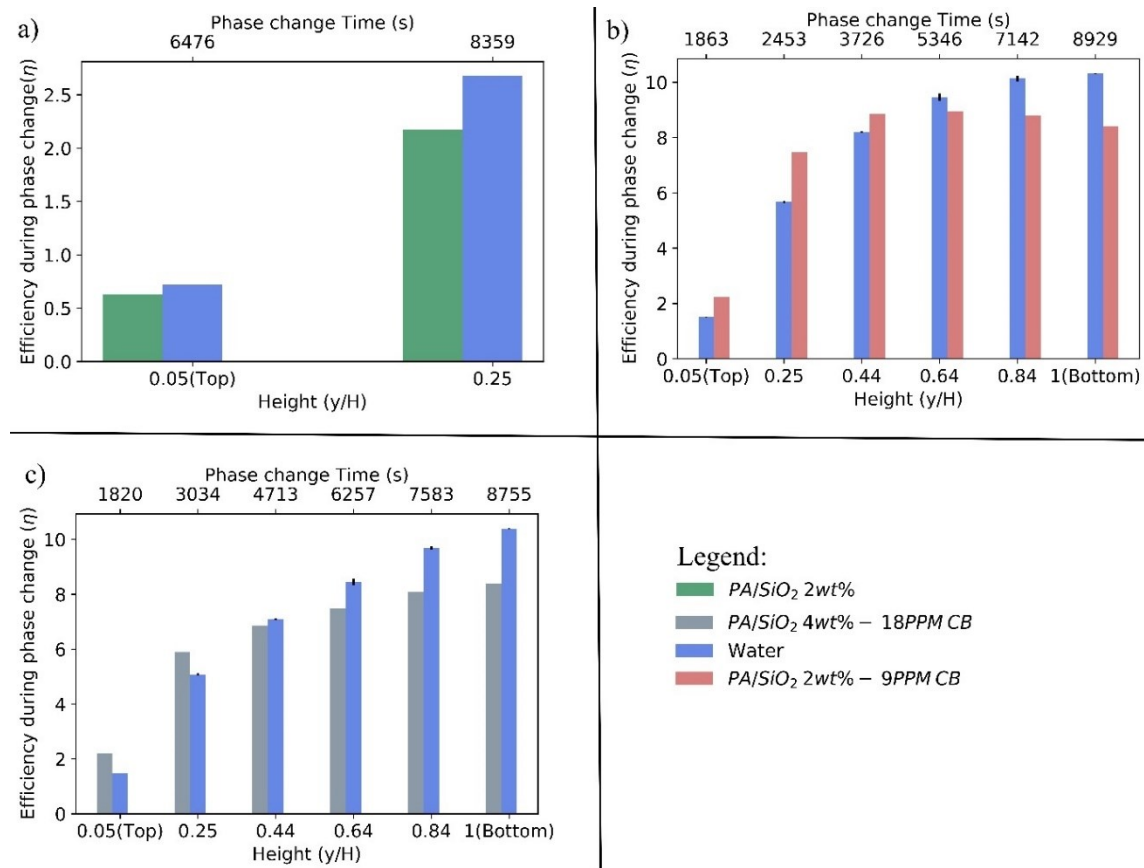


Figure 3.13: Efficiencies during phase change at different heights (represented in the bottom x-axis) and the corresponding phase change time (represented in the top x-axis), for a) pure  $PA/SiO_2$ , b)  $PA/SiO_2$  2wt%-9PPM CB slurry, and c)  $PA/SiO_2$  4wt%-18PPM CB slurry; in comparison with water.

## Chapter 4

### Conclusions and Recommendations

In this chapter, the research questions mentioned in chapter 1 will be answered. A lab-scale stationary state direct absorption solar collector has been designed and installed successfully. A series of photo-thermal experiments were performed to investigate the performance of slurries including both sensible and latent heat storage. The effects of parameters like collector height, irradiation time, and existence of thermal storage on the collector efficiency have been studied. The conclusions and recommendations will be presented in the following sections.

#### 4.1 Conclusions

A laboratory version of a stationary state DASC experimental set up is designed to perform the photo-thermal experiments. The temperature data collected during the experiment is analyzed, and the effects of the different operating parameters like receiver height, and irradiation time on collector performance are studied. The effect of thermal storage on collector performance is also outlined.

Initially, photothermal experiments were performed at 1sun intensity. In comparison to water, at the end of 9000s of irradiation, the carbon black nanofluids temperature improved by 22.35% and 11.24%, respectively at  $y/H=0.05$  (top of the collector) and  $y/H=1$  (bulk volume/ bottom of the collector). On the other hand, the  $Pa/SiO_2$  10wt%- 45PPM carbon black slurry temperature incremented by 11.72% at the top of the collector. But, the bottom temperature was comparable to that of water; this is because of the reduced transmittance of light in the slurry.

The enhancement in temperature is mainly due to the added carbon black particles, acting as an effective photon capture and molecular heater. The added nanoparticle helps to achieve high temperature at a faster rate, but if more particles are used then the lower part of the collector receives less radiation due to attenuation of light along the height of the collector, thereby affecting the performance. On further experiments at the same intensity, the maximum temperature reached by the slurries was 50.3°C at top of the collector, after 6 hours of illumination, far below the peak phase change temperature of 63.1°C. Therefore, to understand the thermal storage behavior of phase change slurries, high intensity beam concentrator was used to achieve the peak phase change temperature at a faster rate.

From the high flux beam concentrator experiments, it can be concluded that with an increase in irradiation time, the temperature increases, but the efficiency decreases. Based on the experiments performed, the carbon black nanofluid reaches high temperature and efficiency compared to base fluid, irrespective of collector height, up to 3000s of irradiation time. For example, at 3000s, the 35PPM carbon black nanofluid temperature change is enhanced by 61.6% and 17.9%, respectively at  $y/H=0.05$  and  $y/H=1$ . This corresponds to collector performance improvement of 1.8 and 1.2 times the efficiency of water. Therefore, for carbon black nanofluids a collector height  $y/H=1$  (30.5mm), yields better performance than water up to 3000s of irradiation.

In the case of  $PA/SiO_2$ -CB slurry, the slurries would have reached high temperatures at the top of the collector, but has a relatively low bulk temperature compared to base fluid, hence the overall performance of the slurry is lower than the base fluid. But, depending on the collector height and irradiation time the slurries reaches a higher temperature than base fluid. For instance, at 600s, the 2wt%-9PPM slurry require a collector of height  $y/H=0.64$  (19.5mm) to achieve a temperature improvement of 13.1%; this resulted in an efficiency improvement of 1.1 times the efficiency of water. With the advancement in time to 3600s, the same efficiency enhancement for 2wt%-9PPM slurry is possible at the collector height  $y/H=0.44$  (13.5mm). Therefore, the required collector height for slurries to perform better than water reduces with further increase in time.

The thermal storage density decrease with increase in height of the collector, because of the increase in the volume of the collector. The energy density increases with time at a given height. The complete collector (volume=21.5ml,  $H=30.5$ mm) takes almost 2.5hours to reach peak phase change temperature. In the case of  $PA/SiO_2$  2wt%-9PPM CB slurry, the efficiency during phase change is more efficient than water up to a collector height of  $y/H=0.44$  (13.5mm). At this collector height and for the illumination of 3600s the 2wt%-9PPM slurry stores 8.26% more energy than water.

To summarize, the photo-thermal slurries comes with advantages and disadvantages in application to DASC. The advantages are the carbon nanoparticles in the slurry helps to reach a high temperature in short duration of time, and the phase change material improves the energy storage density of the slurries. The limitations are photo-thermal slurries performance is limited to the collector height and irradiation time, and a large amount of heat source is required to achieve peak phase change temperature at a faster rate.

Investigating the experimental results of the slurries, for up to an hour of irradiation shows that the maximum collector height of 7.5mm is found to have a better performance than water. Additionally, at these operating conditions, the latent heat is also contributed to the overall performance of the photo-thermal slurries.

## 4.2 Recommendations

- Further research into the optical properties of the prepared sample, helps better to understand the photo-thermal behavior.
- More experiments need to be performed by varying the nanoparticles and PCM, to determine the optimum particle concentration for a particular application.
- To verify the latent heat storage, larger concentration of PCM should be considered while making the slurry.
- Different PCM with low phase transition temperature can be used for low temperature applications.
- The area of the collector is inversely related to efficiency, to further optimize the collector dimensions, diameter can be altered.
- Different nanomaterial with higher thermal conductivity can be employed, currently two nanomaterial in the slurry are being studied. More than two nanomaterial, each having different absorption spectrum can be employed, there by trying to utilize the complete solar spectrum effectively.

## References

- [1] M. Imtiaz Hussain, C. Ménézo, and J.-T. Kim, “Advances in solar thermal harvesting technology based on surface solar absorption collectors: A review,” *Sol. Energy Mater. Sol. Cells*, vol. 187, pp. 123–139, Dec. 2018.
- [2] P. Raj and S. Subudhi, “A review of studies using nanofluids in flat-plate and direct absorption solar collectors,” *Renew. Sustain. Energy Rev.*, vol. 84, pp. 54–74, Mar. 2018.
- [3] BP, “BP statistical review of world energy,” 2018.
- [4] Intentional Energy Agency, “WEO.” [Online]. Available: <https://www.iea.org/weo/>. [Accessed: 19-Apr-2019].
- [5] X. Wang, Y. He, Y. Hu, G. Jin, B. Jiang, and Y. Huang, “Photothermal-conversion-enhanced photocatalytic activity of flower-like CuS superparticles under solar light irradiation,” *Sol. Energy*, vol. 170, no. June, pp. 586–593, 2018.
- [6] X. Wang, C. Li, and T. Zhao, “Fabrication and characterization of poly(melamine-formaldehyde)/silicon carbide hybrid microencapsulated phase change materials with enhanced thermal conductivity and light-heat performance,” *Sol. Energy Mater. Sol. Cells*, vol. 183, pp. 82–91, Aug. 2018.
- [7] T. P. Otanicar, P. E. Phelan, R. S. Prasher, G. Rosengarten, and R. A. Taylor, “Nanofluid-based direct absorption solar collector,” *J. Renew. Sustain. Energy*, vol. 2, no. 3, p. 033102, May 2010.
- [8] C. Silvi and / Swc, “The Role of History in Rediscovering the Lost Culture of Solar Energy; The Role of History in Rediscovering the Lost Culture of Solar Energy,” 2015.
- [9] J. Liu, L. Chen, X. Fang, and Z. Zhang, “Preparation of graphite nanoparticles-modified phase change microcapsules and their dispersed slurry for direct absorption solar collectors,” *Sol. Energy Mater. Sol. Cells*, vol. 159, pp. 159–166, Jan. 2017.
- [10] K. Farhana *et al.*, “Improvement in the performance of solar collectors with nanofluids — A state-of-the-art review,” *Nano-Structures & Nano-Objects*, vol. 18, p. 100276, Apr. 2019.
- [11] X. Ma, Y. Liu, H. Liu, L. Zhang, B. Xu, and F. Xiao, “Fabrication of novel slurry containing graphene oxide-modified microencapsulated phase change material for direct absorption solar collector,” *Sol. Energy Mater. Sol. Cells*, vol. 188, pp. 73–80, Dec. 2018.
- [12] H. K. Gupta, G. Das Agrawal, and J. Mathur, “Investigations for effect of Al<sub>2</sub>O<sub>3</sub>–H<sub>2</sub>O nanofluid flow rate on the efficiency of direct absorption solar collector,” *Case Stud. Therm. Eng.*, vol. 5, pp. 70–78, Mar. 2015.
- [13] P. E. Glaser, “Power from the sun:Its Future,” *Science (80-. )*, vol. 162, no. 3856, 1968.
- [14] X. Ma, Y. Liu, H. Liu, L. Zhang, B. Xu, and F. Xiao, “Fabrication of novel slurry containing graphene oxide-modified microencapsulated phase change material for direct absorption solar collector,” *Sol. Energy Mater. Sol. Cells*, vol. 188, no. August, pp. 73–80, 2018.

- [15] F. Wang, J. Liu, X. Fang, and Z. Zhang, "Graphite nanoparticles-dispersed paraffin/water emulsion with enhanced thermal-physical property and photo-thermal performance," *Sol. Energy Mater. Sol. Cells*, vol. 147, pp. 101–107, Apr. 2016.
- [16] Y. Tian and C. Y. Zhao, "A review of solar collectors and thermal energy storage in solar thermal applications," *Appl. Energy*, vol. 104, pp. 538–553, Apr. 2013.
- [17] Y. Chen, Q. Zhang, X. Wen, H. Yin, and J. Liu, "A novel CNT encapsulated phase change material with enhanced thermal conductivity and photo-thermal conversion performance," *Sol. Energy Mater. Sol. Cells*, vol. 184, no. April, pp. 82–90, 2018.
- [18] M. Mehrali, M. K. Ghatkesar, and R. Pecnik, "Full-spectrum volumetric solar thermal conversion via graphene/silver hybrid plasmonic nanofluids," *Appl. Energy*, vol. 224, pp. 103–115, Aug. 2018.
- [19] S. A. Kalogirou, "Solar thermal collectors and applications," *Prog. Energy Combust. Sci.*, vol. 30, no. 3, pp. 231–295, Jan. 2004.
- [20] P. Phelan, T. Otanicar, R. Taylor, and H. Tyagi, "Trends and Opportunities in Direct-Absorption Solar Thermal Collectors," *J. Therm. Sci. Eng. Appl.*, vol. 5, no. 2, p. 021003, May 2013.
- [21] R. C. Shende and S. Ramaprabhu, "Application of Few-Layered Reduced Graphene Oxide Nanofluid as a Working Fluid for Direct Absorption Solar Collectors.," *J. Nanosci. Nanotechnol.*, vol. 17, no. 2, pp. 1233–239, Feb. 2017.
- [22] H. Tyagi, P. Phelan, and R. Prasher, "Predicted Efficiency of a Low-Temperature Nanofluid-Based Direct Absorption Solar Collector," *J. Sol. Energy Eng.*, vol. 131, no. 4, p. 041004, Nov. 2009.
- [23] J. E. Minardi and H. N. Chuang, "Performance of a 'black' liquid flat-plate solar collector," *Sol. Energy*, vol. 17, no. 3, pp. 179–183, Jul. 1975.
- [24] X. Li, C. Zou, L. Zhou, and A. Qi, "Experimental study on the thermo-physical properties of diathermic oil based SiC nanofluids for high temperature applications," *Int. J. Heat Mass Transf.*, vol. 97, pp. 631–637, Jun. 2016.
- [25] C.-Y. Lin, J.-C. Wang, and T.-C. Chen, "Analysis of suspension and heat transfer characteristics of Al<sub>2</sub>O<sub>3</sub> nanofluids prepared through ultrasonic vibration," *Appl. Energy*, vol. 88, no. 12, pp. 4527–4533, Dec. 2011.
- [26] D. P. Kulkarni, D. K. Das, and R. S. Vajjha, "Application of nanofluids in heating buildings and reducing pollution," *Appl. Energy*, vol. 86, no. 12, pp. 2566–2573, Dec. 2009.
- [27] R. Saidur, K. Y. Leong, and H. A. Mohammad, "A review on applications and challenges of nanofluids," *Renew. Sustain. Energy Rev.*, vol. 15, no. 3, pp. 1646–1668, Apr. 2011.
- [28] E. Sani *et al.*, "Carbon nanohorns-based nanofluids as direct sunlight absorbers," *Opt. Express*, vol. 18, no. 5, p. 5179, Mar. 2010.
- [29] E. Sani *et al.*, "Potential of carbon nanohorn-based suspensions for solar thermal collectors," *Sol. Energy Mater. Sol. Cells*, vol. 95, no. 11, pp. 2994–3000, Nov. 2011.
- [30] B. Zalba, J. M. Marín, L. F. Cabeza, and H. Mehling, "Review on thermal energy

- storage with phase change: materials, heat transfer analysis and applications,” *Appl. Therm. Eng.*, vol. 23, no. 3, pp. 251–283, Feb. 2003.
- [31] D. Zhou, C. Y. Zhao, and Y. Tian, “Review on thermal energy storage with phase change materials (PCMs) in building applications,” *Appl. Energy*, vol. 92, pp. 593–605, Apr. 2012.
- [32] M. M. Farid, A. M. Khudhair, S. A. K. Razack, and S. Al-Hallaj, “A review on phase change energy storage: materials and applications,” *Energy Convers. Manag.*, vol. 45, no. 9–10, pp. 1597–1615, Jun. 2004.
- [33] K. Yuan, H. Wang, J. Liu, X. Fang, and Z. Zhang, “Novel slurry containing graphene oxide-grafted microencapsulated phase change material with enhanced thermo-physical properties and photo-thermal performance,” *Sol. Energy Mater. Sol. Cells*, vol. 143, pp. 29–37, Dec. 2015.
- [34] Z. Chen, J. Wang, F. Yu, Z. Zhang, and X. Gao, “Preparation and properties of graphene oxide-modified poly(melamine-formaldehyde) microcapsules containing phase change material n-dodecanol for thermal energy storage,” *J. Mater. Chem. A*, vol. 3, no. 21, pp. 11624–11630, May 2015.
- [35] Y. Zhang, X. Zheng, H. Wang, and Q. Du, “Encapsulated phase change materials stabilized by modified graphene oxide,” *J. Mater. Chem. A*, vol. 2, no. 15, p. 5304, Mar. 2014.
- [36] Insulcon, “Technical Datasheet REFRACTORY FIBER PRODUCTS Technical Datasheet.”
- [37] S. T. Latibari, R. Cuypers, J. W. O. Salari, Amir.H.Mahmoudi, and Mina.Shahi, “Preparation and Characterization of Heat Transfer Fluid for Application in Direct Absorption Solar Collectors.”
- [38] M. Chen, Y. He, J. Zhu, and D. Wen, “Investigating the collector efficiency of silver nanofluids based direct absorption solar collectors,” *Appl. Energy*, vol. 181, pp. 65–74, Nov. 2016.
- [39] J. Liu, Z. Ye, L. Zhang, X. Fang, and Z. Zhang, “A combined numerical and experimental study on graphene/ionic liquid nanofluid based direct absorption solar collector,” *Sol. Energy Mater. Sol. Cells*, vol. 136, pp. 177–186, May 2015.



## Appendix A1 Solar Simulator

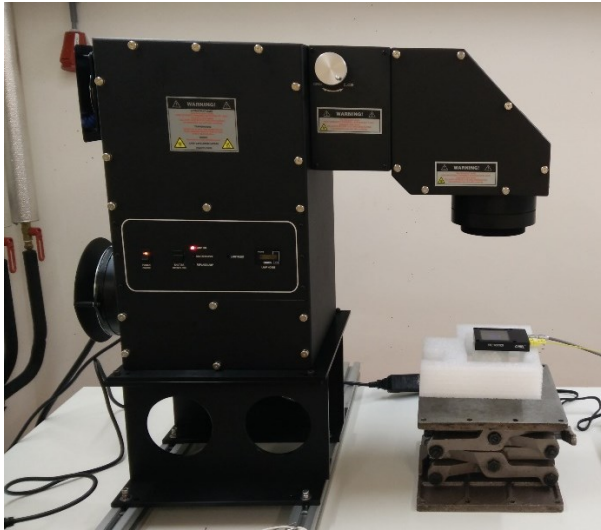


Figure A1.1 :Installed solar simulator without beam concentrator.

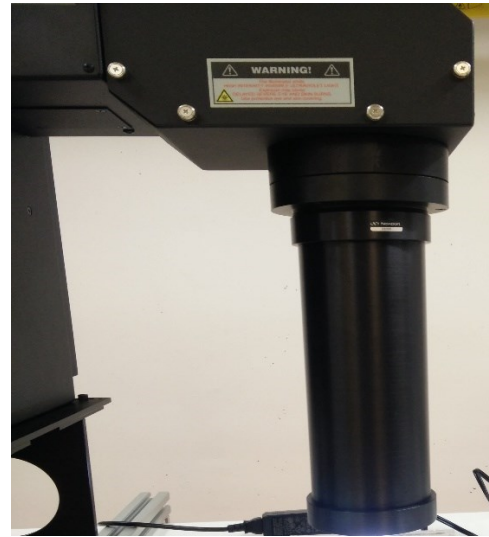


Figure A1.2: Solar simulator with beam concentrator.

**Table A1.1: Performance and technical specifications of the solar simulator.**

	Standards			Sol3A Performance
	IEC 60904-9 ED2 Class A	JIS Class A	ASTM Class A	Model: 94023A
<b>Spectral Match</b>	0.75-1.25% fraction of ideal percentage.	0.75-1.25% fraction of ideal percentage.	0.75-1.25% fraction of ideal percentage.	Class AAA
<b>Non-Uniformity of Irradiance</b>	<2.0%	±2%	2%	Class AAA
<b>Temporal Instability</b>	<0.5% short term instability. <2.0% long term instability.	±1%	±2%	Class AAA
<b>Electrical Specifications</b>	<b>Solar Simulator</b>	AC input: 95-264VAC, 47-63Hz; 3A maximum current.		
	<b>Power supply</b>	AC input: 95-264VAC, 47-63Hz; 12A maximum current.		
<b>Output Beam</b>	51x51 mm			

<b>Lamp Type</b>	Xenon, ozone free	
<b>Lamp Wattage</b>	450 W	
<b>Average Lamp Life</b>	1000 h	
<b>Horizontal Intensity</b>	1300 cd	

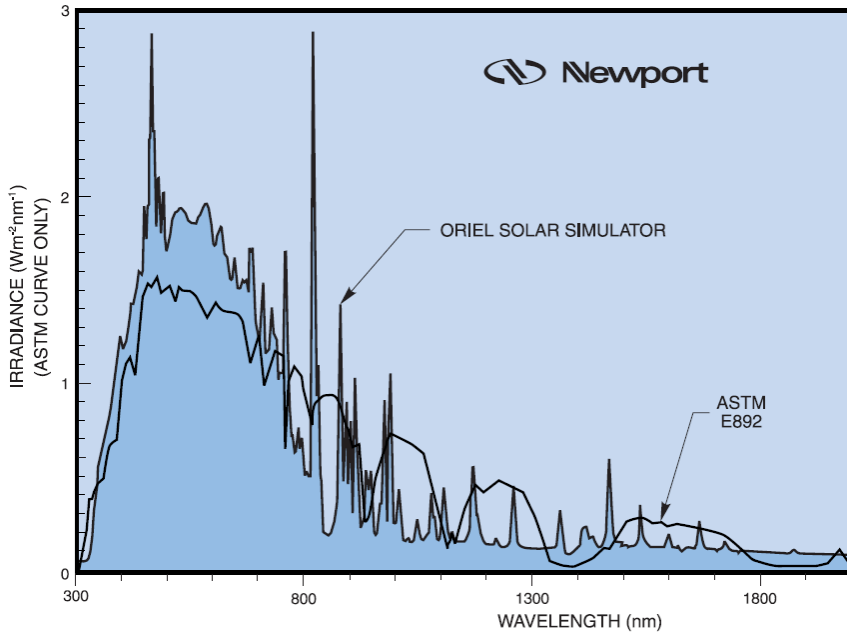


Figure A1.3: Spectral distribution of AM1.5G simulators normalized to ASTM E892 standard spectrum [44].

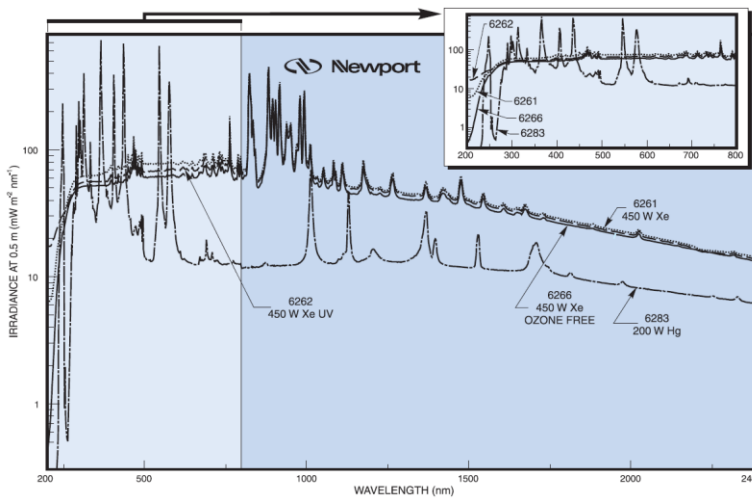


Figure A1.4: Spectral irradiance of 450W xenon bulbs [43].

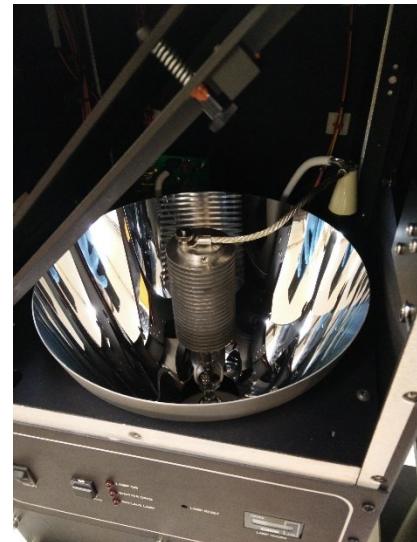


Figure A1.5: Installed 450W xenon ozone free lamp with heat sink.

**Spectral match:** It is measured by using a calibrated spectroradiometer with a grating monochromator and a discrete detector. The spectral match of the Sol3A performed by Newport is as shown below.

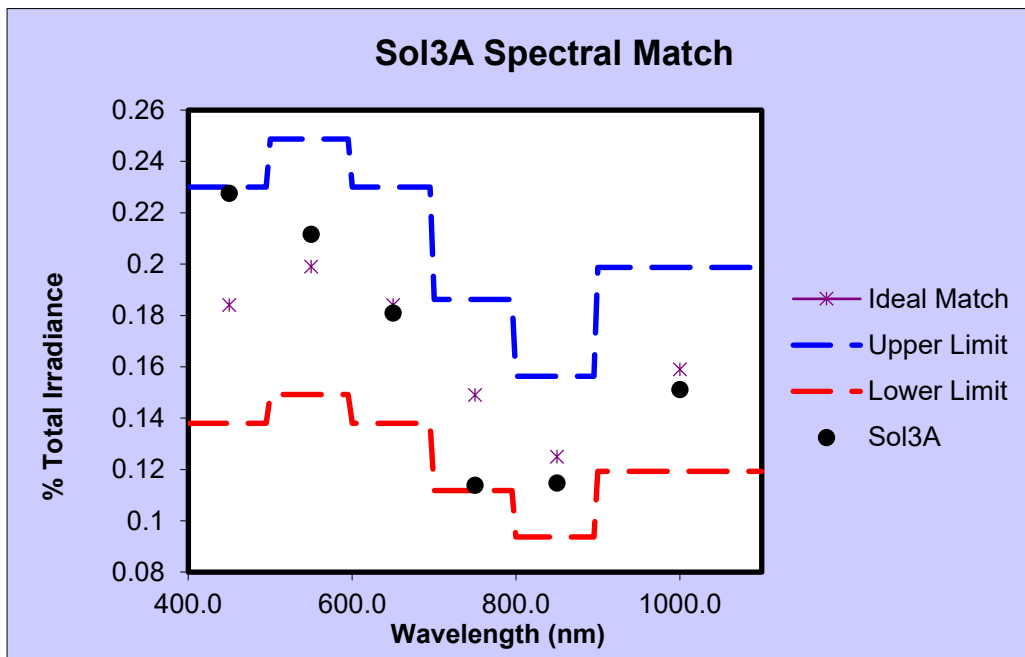


Figure A1.6: Spectral match of Sol3A solar simulator [42].

**Non-Uniformity:** non-uniformity is defined as

$$Non - Uniformity (\%) = \frac{(Max\ irradiance - Min\ irradiance)}{(Max\ irradiance + Min\ irradiance)} * 100\% \quad \text{Eq A1.1}$$

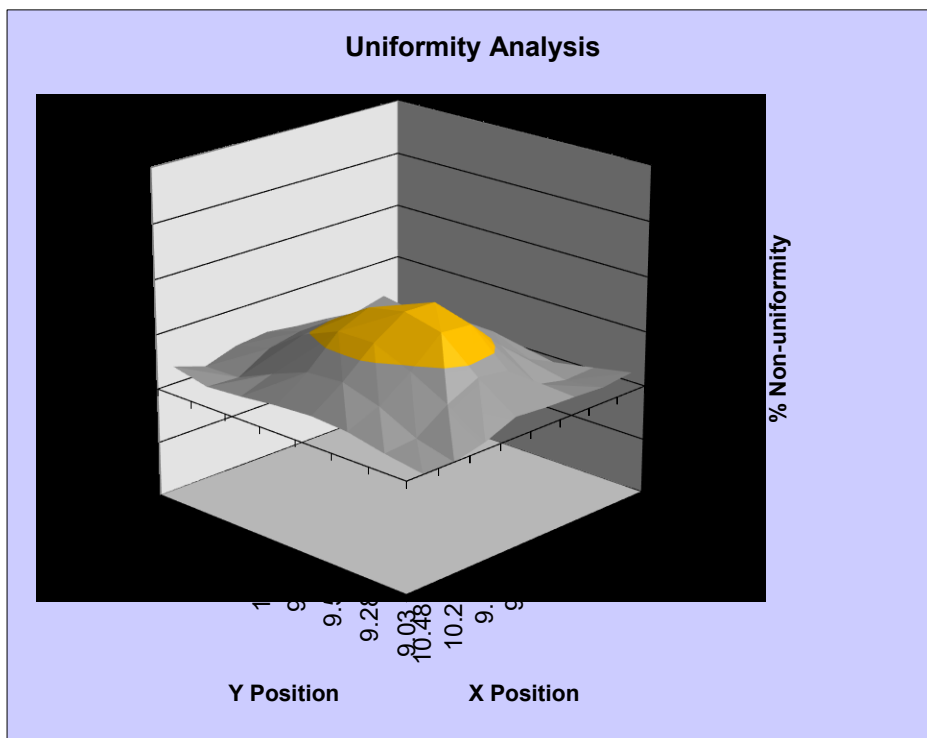


Figure A1.7: Non-uniformity of sol3A simulator[42].

**Temporal instability:** Temporal instability is defined as

$$\text{Temporal instability (\%)} = \frac{(\text{Max irradiance} - \text{Min irradiance})}{(\text{Max irradiance} + \text{Min irradiance})} * 100\% \quad \text{Eq A1.2}$$

Temporal instability is measured by taking 20 samples per second for 60 seconds.

**Table A1.2: Percentage change in non-uniformity with partial sun attenuator installed on sol3A solar simulator [42].**

Condition	Non-uniformity %
Normal 1 sun- no partial sun module installed.	1.33
Fully open 1 sun – with partial sun attenuator installed.	1.25
0.75 sun- with partial sun attenuator installed.	1.80
0.50 sun- with partial sun attenuator installed.	2.40
0.25 sun- with partial sun attenuator installed.	3.97
Fully closed 0.11 sun – with partial sun attenuator installed.	5.35

**Safety Precautions and Measures:** The following safety precautions must be ensured while setting up and operating the solar illuminator.

- Wear UV protective safety glasses.
- Wear UV protective gloves, while handling an arc lamp, and operating the simulator.
- Cover all exposed skin and avoid exposure to direct, reflected or diffuse radiation from the lamp.
- Incorrect terminal connections to the simulator can be hazardous and may result in violent lamp explosion.
- Care must be taken while installing or remounting the solar simulator on a work surface, as there are chances of it leaning forwards due to the shift in the center of gravity to the front of the unit.
- Don't try to override the safety interlocks.
- Don't operate the lamp unless all housing panels are in place.
- Do not attempt to quick restart the lamp, until the lamp has completely cooled. This can have significant effect on lamp life.
- Don't look directly into the output beam, because the simulator produces high intensity ultraviolet radiation. This radiation possess the risk of melanoma and formation of cataracts with repeated exposure to skin and outer layers of the eye.
- Provide adequate ventilation to remove ozone produced during the normal operation of the simulator
- After few minutes of operation, arc lamp can reach high temperatures up to 220°C and even after turning off, it remains quite hot for at least 25-30 minutes. Therefore, avoid touching any surfaces of the simulator.
- Arc lamp ignition requires high voltage pulse and hence good electromagnetic interference shielding may be necessary to protect sensitive circuitry.

## Appendix A2 Other Components

**Table A2.1: Specifications of quartz window.**

Diameter	50.8mm
Thickness	12mm
Substrate	UV fused silica
Parallelism	$\leq 5$ arcsec
Wavelength range	185 nm to 2.1 $\mu$ m
Index of refraction	1.458
Density	$2.203 \frac{g}{cm^3}$
Coefficient of thermal expansion	$0.55 \times 10^{-6} / ^\circ C$
Heat capacity	0.736 J/(g * K)

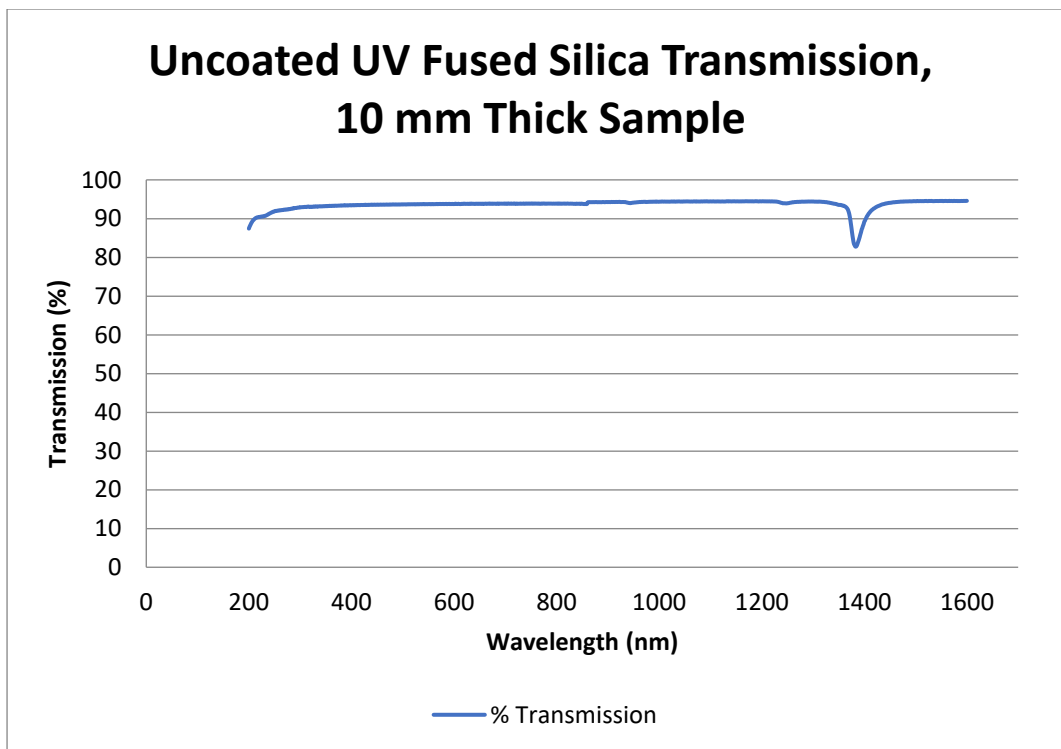


Figure A2.1: Transmission of light through uncoated UV fused silica window.



Figure A2.2: Quartz window.

**Table A2.2: Specifications of Collector.**

Inner cylinder diameter	30 mm
Inner cylinder height	30.5mm
Distance between the thermocouples.	
T6-T5	5 mm
T5-T4	6 mm
T4-T3	6 mm
T3-T2	6 mm
T2-T1	5.8 mm



Figure A2.3: Isometric view of the collector.



Figure A2.4: 3D printed collector.

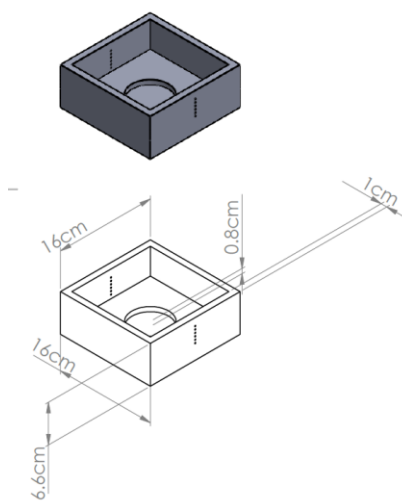


Figure A2.5: Collector holder design.

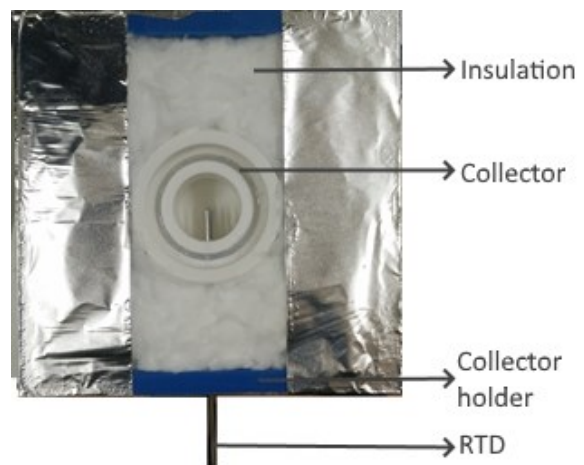


Figure A2.6: 3D printed collector holder with collector and insulation.

**Table A2.3: Specifications of RTD Pt-100.**

Permitted deviation	Class A - $\pm(0.15 + 0.002 * t)$ °C
Sheath diameter	3 mm
Insulation material	High purity magnesium oxide.
Sheath material	Stainless steel.
Circuitry	3 wire from measuring resistor.



Figure A2.7: DAQ system with transmitters.

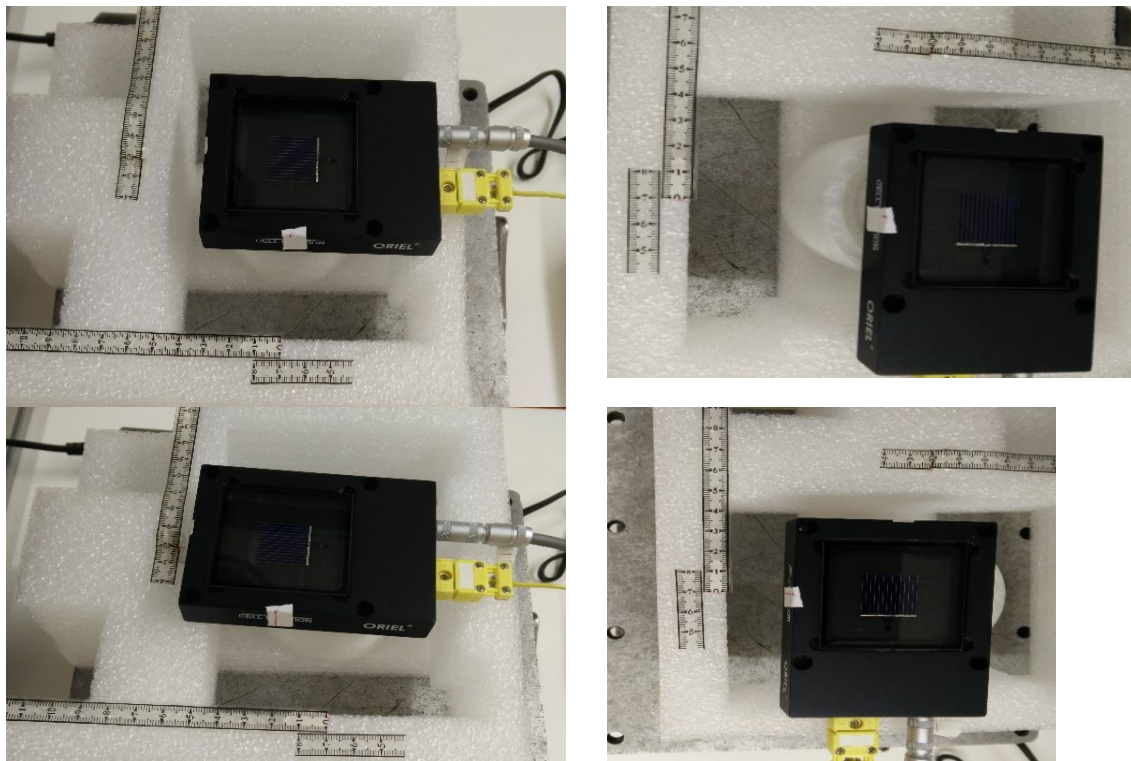


Figure A2. 8: Solar simulator intensity measurement set up.

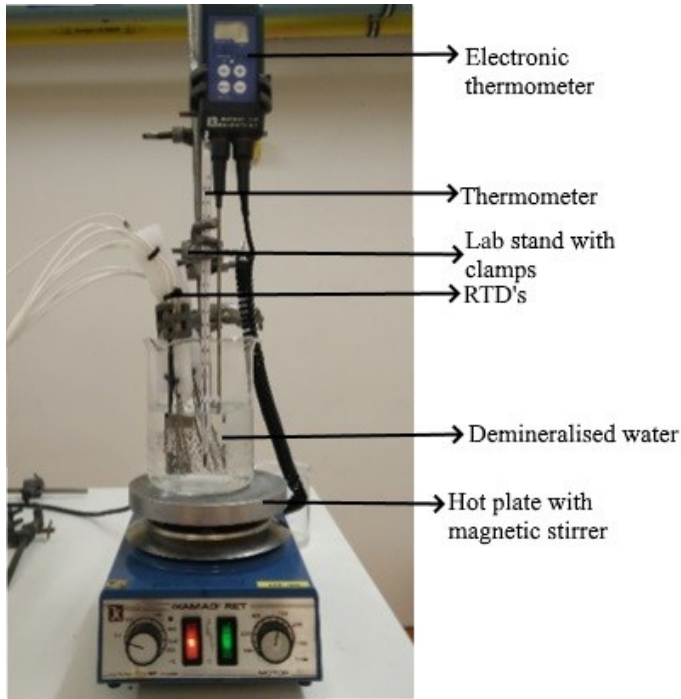


Figure A2.9: RTD calibration set up.



Figure A2.10: RTD calibration at 0°C.

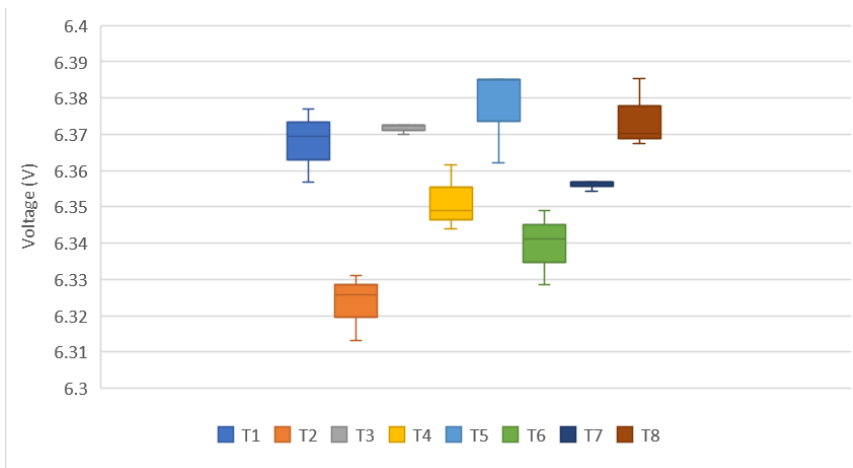


Figure A2.11: Measured voltage standard deviation of 3 trials for all the RTD used in the photothermal experiment. Maximum standard deviation is within 3.5%.

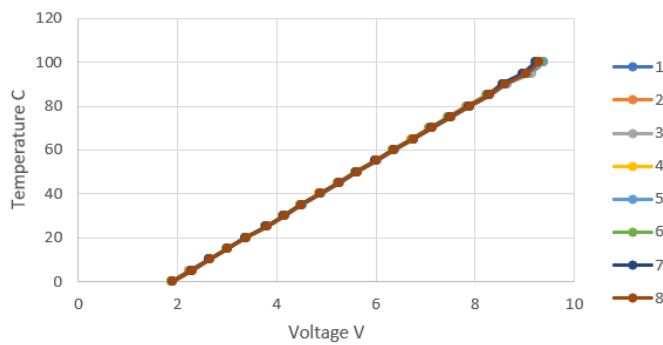


Figure A2.12: Temperature as a function of voltage for all the 8 RTD.

## Appendix A3

### Materials

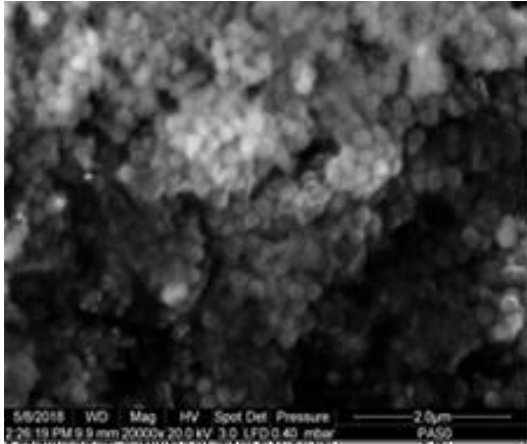


Figure A3.1: SEM image of palmitic acid.

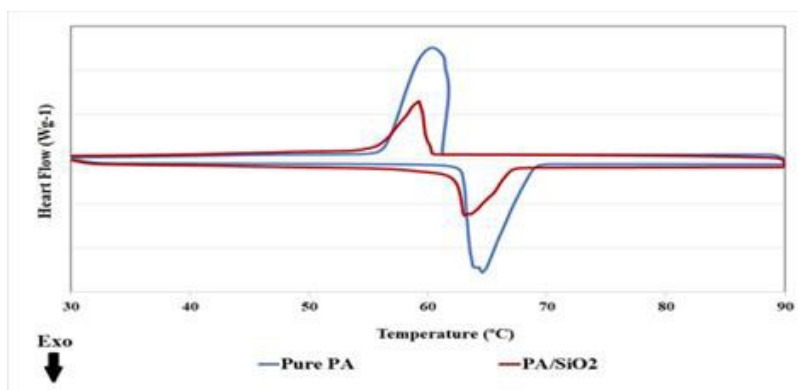


Figure A3.2: DSC of palmitic acid.

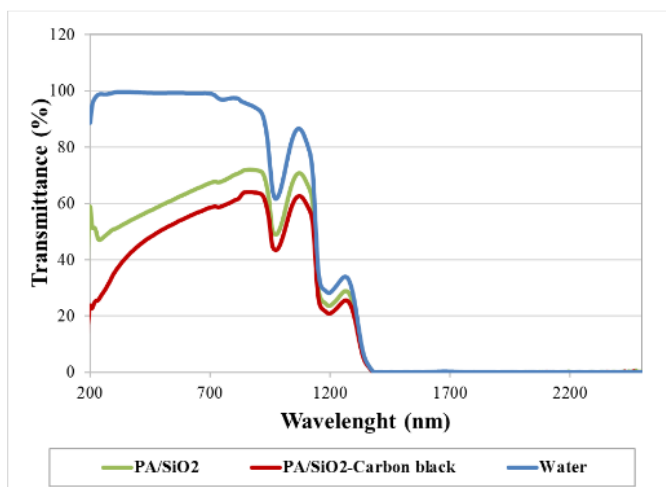


Figure A3.3: Transmittance spectra of water, palmitic acid and photothermal slurry.



